Alone on a wide wide sea. The origin of SECCO 1, an isolated star-forming gas cloud in the Virgo cluster*†‡

M. Bellazzini,[1]★ L. Armillotta,[2] S. Perina,[3] L. Magrini,[4] G. Cresci,[4] G. Beccari,[5] G. Battaglia,[6,7] F. Fraternali,[8,9] P. T. de Zeeuw,[10,11] N. F. Martin,[12,13] F. Calura,[1] R. Ibata,[12] L. Coccato,[5] V. Testa[14] and M. Correnti[15]

[1]*INAF-Osservatorio di Astrofisica e Scienza dello Spazio di Bologna, Via Gobetti 93/3, I-40129 Bologna, Italy*
[2]*Research School of Astronomy and Astrophysics – The Australian National University, Canberra ACT 2611, Australia*
[3]*INAF-Osservatorio Astronomico di Torino, Via Osservatorio 30, I-10025 Pino Torinese, Italy*
[4]*INAF-Osservatorio Astrofisico di Arcetri, Largo E. Fermi 5, I-50125 Firenze, Italy*
[5]*European Southern Observatory, Karl-Schwarzschild-Strasse 2, D-85748 Garching bei München, Germany*
[6]*Instituto de Astrofisica de Canarias, E-38205 La Laguna, Tenerife, Spain*
[7]*Universidad de La Laguna, Dpto. Astrofisica, E-38206 La Laguna, Tenerife, Spain*
[8]*Kapteyn Astronomical Institute, University of Groningen, Postbus 800, NL-9700 AV Groningen, the Netherlands*
[9]*Dipartimento di Fisica and Astronomia, Università degli Studi di Bologna, Viale Berti Pichat, 6/2, I-40127 Bologna, Italy*
[10]*Leiden Observatory, Leiden University, Postbus 9513, NL-2300 RA Leiden, the Netherlands*
[11]*Max Planck Institut für extraterrestrische Physik, Giessenbachstrasse, D-85748 Garching, Germany*
[12]*Université de Strasbourg, CNRS, UMR 7550, F-67000 Strasbourg, France*
[13]*Max-Planck-Institut für Astronomie, Königstuhl 17, D-69117 Heidelberg, Germany*
[14]*INAF-Osservatorio Astronomico di Roma, via Frascati 33, I-00040 Monteporzio, Italy*
[15]*Space Telescope Science Institute, Baltimore, MD 21218, USA*

ABSTRACT

SECCO 1 is an extremely dark, low-mass ($M_\star \simeq 10^5$ M$_\odot$), star-forming stellar system lying in the low-velocity cloud (LVC) substructure of the Virgo cluster of galaxies, and hosting several H II regions. Here, we review our knowledge of this remarkable system, and present the results of (a) additional analysis of our panoramic spectroscopic observations with MUSE, (b) the combined analysis of *Hubble Space Telescope* and MUSE data, and (c) new narrow-band observations obtained with OSIRIS@GTC to search for additional H II regions in the surroundings of the system. We provide new evidence supporting an age as young as $\lesssim 4$ Myr for the stars that are currently ionizing the gas in SECCO 1. We identify only one new promising candidate H II region possibly associated with SECCO 1, thus confirming the extreme isolation of the system. We also identify three additional candidate pressure-supported dark clouds in Virgo among the targets of the SECCO survey. Various possible hypotheses for the nature and origin of SECCO 1 are considered and discussed, also with the help of dedicated hydrodynamical simulations showing that a hydrogen cloud with the characteristics of SECCO 1 can likely survive for $\gtrsim 1$ Gyr while travelling within the LVC Intra Cluster Medium.

Key words: H II regions – galaxies: clusters: individual: Virgo cluster – galaxies: dwarf – galaxies: interactions – galaxies: star formation.

1 INTRODUCTION

SECCO 1 is a faint star-forming stellar system that was discovered by Bellazzini et al. (2015a,b, B15a and B15b, hereafter) in a survey (SECCO;[1] B15a) aimed at searching for stellar counterparts of Ultra Compact High Velocity H I clouds (UCHVCs), selected from the ALFALFA (Adams, Giovanelli & Haynes 2013) radio survey.

[1] http://www.bo.astro.it/secco

Table 1. Physical properties of SECCO 1 (assuming $D = 17.0$ Mpc).

Parameter	MB	SB	Total	Note
RA$_{J2000}$	12:21:54.0	12:21:55.7		from the ACS-WFC F606W image[a]
Dec.$_{J2000}$	+13:27:36.8	+13:29:02.3		from the ACS-WFC F606W image[a]
$L_V[L_{V,\odot}]$	$1.2^{+0.5}_{-0.4} \times 10^6$	$4.4^{+2.6}_{-1.6} \times 10^5$	$1.6^{+0.6}_{-0.4} \times 10^6$	from Be17a
$M_\star[\mathrm{M}_\odot]$	$\lesssim 1.2 \times 10^5$	$\lesssim 0.4 \times 10^5$	$\lesssim 1.6 \times 10^5$	upper limit from integrated light (Be17a)
$M_\star[\mathrm{M}_\odot]$	$7.3^{+3.0}_{-2.4} \times 10^4$	$2.7^{+1.6}_{-1.0} \times 10^4$	$1.0^{+0.4}_{-0.3} \times 10^5$	from integrated light (Be17a)[b]
$M_\star[\mathrm{M}_\odot]$	$5.4 \pm 1.3 \times 10^4$			from CMD analysis (S17)
$M_{\mathrm{H\,I}}[\mathrm{M}_\odot]$	1.5×10^7	3.6×10^6	1.9×10^7	from A15[c]
Radial size$_\star$ [kpc]	1.2	1.2		radius enclosing all the Hα emission (Be17a)
$r_{\mathrm{H\,I}}$ [kpc]	3.7	<1.6		H I radius from A15
$V_h^\star$ [km s^{-1}]	-153.2 ± 1.4	-126.5 ± 2.5		heliocentric radial velocity (stars, Be17a)
$V_h^{\mathrm{H\,I}}$ [km s^{-1}]	-142	-123		heliocentric radial velocity (H I, A15)
$\sigma_{V_h}^\star$ [km s^{-1}]	3.5 ± 2.1	2.7 ± 5		from Be17a
$\sigma_{V_h}^{\mathrm{H\,I}}$ [km s^{-1}]	9 ± 3	4 ± 2		from A15
$\langle 12 + log(O/H)\rangle$	8.37 ± 0.11	8.39 ± 0.11	8.38 ± 0.11	from Be17a,b
SFR [M$_\odot$ yr^{-1}]			$0.7 \pm 0.2 \times 10^{-3}$	from Hα flux (Be17a,b)[d]
SFR [M$_\odot$ yr^{-1}]			1.1×10^{-3}	from CMD analysis (S17)
D_p(MB-SB) [kpc]			7.3	proj. distance between MB and SB
D_p(stars-H I) [kpc]	$\simeq 0.0$	$\simeq 2.5$		proj. distance between stars and gas cloud
D_p(MB-NGC4299) [kpc]	582			proj. distance from proposed parent system (Be17a)
D_p(MB-M86) [kpc]	346			proj. distance from proposed parent system (S17)
D_p(MB-IC3142) [kpc]	255			proj. distance from proposed parent system (this work)

Notes. [a]Geometric centres of the distribution of sources, estimated by eye. For MB, this is slightly different than that adopted in Be17a that referred to the centre of the main northern clump of sources. To establish the geometric centre of SB, we used the distribution of H II regions on the MUSE data cube as a guideline.

[b]Adopting $M/L_V = 0.061$ from the solar-scaled BASTI model (Percival et al. 2009) with an age = 30 Myr and [Fe/H] = -0.66.

[c]The H I cloud AGC229490 is off-set by 0.5 arcmin from SB.

[d]The reported uncertainty combines the error on the integrated Hα flux and the uncertainty associated with the adopted calibration (Kennicutt 1998). Varying the assumed distance by ± 3.0 Mpc changes the SFR by $\simeq \pm 0.2 \times 10^{-3}$ M$_\odot$ yr^{-1}.

In B15b, we proved the physical association of the small group of blue compact sources originally identified in B15a with the UCHVC HVC 274.68+74.0, from the sample of Adams et al. (2013), and we obtained a first estimate of the oxygen abundance, which appeared anomalously high for a dwarf galaxy as faint as SECCO 1. Subsequently, Sand et al. (2015, S15, hereafter) reported on the independent discovery of the same system, confirming the results of B15b. These authors identified a smaller system with similar appearance lying just ∼2 arcmin apart (see also Beccari et al. 2016, Be16, hereafter). In the following, we will refer to the two pieces of SECCO 1 as the Main Body (MB) and the Secondary Body (SB), according to Beccari et al. (2017a, Be17a, hereafter). Both B15b and S15 agree that SECCO 1 lies within the Virgo cluster of galaxies. In particular, it probably belongs to a substructure of the cluster known as low-velocity cloud (LVC; Boselli et al. 2014), whose central galaxy is the spiral NGC 4216. The *Hubble Space Telescope* (*HST*) photometry of SECCO 1 obtained by Sand et al. (2017, S17, hereafter) is consistent with this conclusion.

High spatial resolution H I observations by Adams et al. (2015, A15, hereafter) split the original HVC 274.68+74.0 into two smaller clouds: AGC 226067, centred on MB, and AGC 229490, off-set by $\simeq 0.5$ arcmin with respect to SB. Assuming a distance $D = 17.0$ Mpc for the LVC (following Boselli et al. 2014), the total H I mass associated with SECCO 1 is $M_{\mathrm{H\,I}} \sim 2 \times 10^7$ M$_\odot$. On the other hand, the total stellar mass derived with two independent methods from *HST* data by Be17a and S17 is $M_\star \lesssim 1.6 \times 10^5$ M$_\odot$, thus implying an H I-to-stellar mass ratio of $\frac{M_{\mathrm{H\,I}}}{M_\star} \gtrsim 100$, fully in the range of almost-dark galaxies (Cannon et al. 2015).[2]

Finally, in Be17a, we presented the results of panoramic optical spectroscopy of SECCO1 MB and SB obtained with the integral-field spectrograph MUSE@VLT (Bacon et al. 2014). The MUSE data cube allowed us to identify many individual H II regions in both MB and SB, measuring their radial velocity and metallicity. We found that MB and SB not only have very similar systemic velocities but also the same oxygen abundance, thus demonstrating that the two systems have a common origin.

In particular, all the H II regions in which we could obtain a reliable estimate of the oxygen abundance have the same abundance (from strong-lines indicators) within the observational uncertainties. The mean metallicity is $\langle 12 + (O/H)\rangle = 8.38 \pm 0.10$, confirming the earlier estimate by B15b, a value typical of galaxies as massive as the Large Magellanic Cloud or M33. The anomalously high metallicity, for the small stellar mass, strongly suggests that the gas that is presently converted into stars in SECCO 1 was chemically enriched in a much larger galaxy, from which it was torn apart by tidal or ram-pressure interaction with the harsh Virgo environment. The apparent lack of a stellar population older than a few tens of Myr provides additional support to this hypothesis (Be17a, S17). The star formation was (independently) found by Be17a,b[3] and by S17 to have a rate typical of star-forming dwarfs with total luminosity comparable to SECCO 1 (James et al. 2015, see Table 1, below).

We feel more confident on the Be17a estimate since there, while summing the light of SECCO 1, we were able to exclude the contribution from unrelated sources that we unambiguously identified, based on their velocity, thanks to the MUSE spectra.

[2] Note that S17 provide an M_V estimate that is 0.9 mag brighter than that by Be17a, but, given the large uncertainties, this corresponds to a 2σ difference.

[3] The SFR originally reported in Be17a was flawed by a trivial computation error that has been corrected in Beccari et al. (2017b).

While star formation is known to occur in ram-pressure stripped gas clouds in galaxy clusters (see e.g. Gerhard et al. 2002; Hester et al. 2010; Fumagalli et al. 2011, 2014; Yoshida et al. 2012; Kenney et al. 2014; Fossati et al. 2016, and references therein) and in the surrounding of interacting galaxies (see e.g. Ryan-Weber et al. 2004), this usually happens in relatively close proximity to the stripped galaxies. SECCO 1 is by far the most isolated case ever observed (S17, Be17a), as the closer plausible progenitor proposed up to now (the M86 subgroup, S17) lies at more than 350 kpc (but see below). This implies that, if indeed SECCO 1 is a gas cloud stripped from that group, it must have travelled within the hot Intra Cluster Medium (ICM) for about 1 Gyr before the ignition of the current star formation episode (Be17a, S17). Hence, SECCO 1 is of special interest to understand the behaviour of such long-lived quiescent stripped clouds that may be present in large numbers within galaxy clusters (Burkhart & Loeb 2016).

In Table 1, we provide a summary of the main physical properties of SECCO 1, adopting the distance $D = 17.0$ Mpc, following A15, Be17a, and S17. This is the distance to SECCO 1 that we always adopt in this paper.

In Be17a, we presented the observational framework for this intriguing stellar system. Here, we discuss and investigate in detail its origin and evolution, with the support of dedicated hydrodynamical simulations. Section 2 is devoted to describe the reduction of the *HST* images of SECCO 1 already presented by S17, and of the deep narrow-band Hα images that we obtained with OSIRIS@GRANTECAN (GTC). In Section 3, we present additional results from the MUSE data, in particular on the effect of the ionization on the estimate of metallicity and on the nature of ionizing sources. In Section 4, we analyse the stellar content of SECCO 1, coupling the constraints from *HST* and MUSE data. In Section 5, we present the results of the GTC Hα imaging. In Section 6, we put SECCO 1 in the context of dwarf galaxies and of stripped gas clouds, discussing the pros and cons of various evolutionary paths. In Section 7, we present the results of 2D and 3D hydrodynamical simulations aimed at establishing the lifetime and evolution of a pressure-supported H I gas cloud similar to SECCO 1 travelling into the ICM. In Section 8, we discuss the conditions for the occurrence of star formation in H I clouds similar to SECCO 1 and we identify three new candidate dark gas clouds that may be wandering within the Virgo ICM like SECCO 1. Finally, in Section 9, we summarize our results.

2 DATA ANALYSIS

In this section, we briefly report on the reduction of the *HST* images of SECCO 1 obtained by S17, which will be discussed in Section 4, and of the acquisition and reduction of narrow-band Hα imaging, whose results are presented in Section 5.

2.1 *HST* photometry

S17 present a detailed analysis of *HST* Advanced Camera for Surveys (ACS) Wide Field Camera (WFC) F606W and F814W images of SECCO 1 (GO 13735 programme; P.I.: D.J. Sand).

We reduced and analysed independently the S17 data set to have a deeper insight on the stellar populations in SECCO 1 by combining the *HST*-ACS and MUSE data. Positions and photometry of individual stars were obtained with the ACS module of the point spread function fitting package DOLPHOT v.2.0 (Dolphin 2000), as described, for example, in Bellazzini et al. (2011b). We adopted a threshold of 2.5σ above the background for the source detection. Photometry

was performed on the individual images corrected for charge transfer efficiency (FLC files), adopting the F814W drizzled distortion-corrected image (DRC file) as the reference for source identification. In the following, we will use magnitudes in the ACS-WFC VEGAMAG system and the analysis will be limited to the best-quality sources, selected by having quality flag=1, sharpness parameter |sharp| < 0.2 for F814W≤26.5 and $-0.4 <$ sharp < 0.2 for F814W>26.5, crowding parameter crowd < 1.0, goodness of fit parameter chi < 2.0, and photometric errors in both passbands ≤0.5 mag. The resulting Colour Magnitude Diagram (CMD) is discussed in Section 4.

2.2 GTC Hα imaging

S17 report that there is no evidence of further pieces of SECCO 1 within the field sampled by their ACS images. However, the ACS-WFC field is relatively small and the most interesting (and easy to find) kinds of sources to be searched for in the surroundings of SECCO 1 are H II regions, isolated or in groups, that can be associated with the system. Indeed, e.g. ram-pressure stripping episodes are expected to produce star-forming blobs in large numbers (see Kapferer et al. 2009, and the discussion in Section 6, below).

To look for these sources, we obtained Hα imaging of an $\simeq 7.8$ arcmin × 7.8 arcmin field centred on SECCO1 MB with the OSIRIS[4] camera mounted on the 10.4-m Gran Telescopio CANARIAS (GTC), at the Observatory Roque de los Muchachos, in La Palma, Spain (programme GTC42-16A; P.I.: G. Battaglia). We used the OSIRIS tunable filters (González et al. 2014) f657/35, sampling Hα rest frame (FWHM$\simeq$ 35 nm), and f680/43, sampling an adjacent portion of the continuum (FWHM$\simeq$ 43.2 nm). We obtained a total of twenty one $t_{exp} = 600$ s images per filter, applying a dithering of a few arcsec between each individual image, in various service mode visits from 2017 January to March. The typical seeing was around ∼1.0 arcsec.

All the images were corrected for flat-field and bias and the sky was subtracted, also removing the sky ring patterns that are typical of this observing mode of OSIRIS (González et al. 2014). Then all the images were combined into one single-stacked f657/35 image and one single-stacked f680/42 image. We used Sextractor (Bertin & Arnouts 1996) to identify sources with peak intensity $\gtrsim 10\sigma$ above the background and to measure their magnitudes (mag$_{H\alpha}$ and mag$_{cont}$) in both images. The output catalogues were combined using codes from the CATAPACK suite.[5] Then, in a plot mag$_{H\alpha}$ versus colour (mag$_{H\alpha}$ − mag$_{cont}$), we identified the sources having an excess in mag$_{H\alpha}$ − mag$_{cont}$ larger than three times the standard deviation in a broad range around their Hα luminosity. In this way, we obtained a catalogue of a handful of candidate Hα emitters, including already known SECCO 1 sources as well as several sources which are detected only in Hα and not in continuum images. The analysis of this catalogue is described in Section 5.

3 MORE FROM MUSE: IONIZATION, KINEMATICS, AND IONIZING SOURCES

As a first step in our review of the properties of SECCO 1, we present some additional analysis of the MUSE data presented in Be17a (see this paper for all the details on the observational material and data reduction). In Fig. 1, we show the position of the individual sources

---

[4] http://www.gtc.iac.es/instruments/osiris/osiris.php

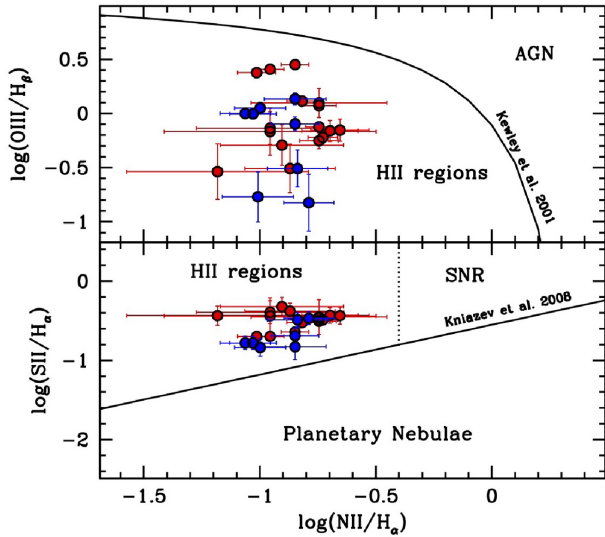[5] By P. Montegriffo, http://davide2.bo.astro.it/∼paolo/Main/CataPack.html.

Figure 1. Classification diagnostic diagrams for all the SECCO 1 sources identified in Be17a for which reliable estimate of the flux for the relevant lines could be obtained, following Kniazev, Pustilnik & Zucker (2008). Red filled circles are sources residing in MB, and blue filled circles lie in SB. The threshold curves are from Kewley et al. (2001, upper panel), and from Kniazev et al. (2008, lower panel). The dotted line in the lower panel marks the lower limit in $\log(N\,\textsc{ii}/H\alpha)$ of the locus occupied by SNRs. The upper(lower) panel includes 24(23) of the 38 sources identified by Be17a.

identified in Be17a in the diagnostic diagrams that are generally used to discriminate H\,\textsc{ii} regions from active galactic nuclei, supernova remnants (SNRs), and planetary nebulae, based on line flux ratios. According to these diagnostic diagrams, all the considered sources are unambiguously classified as H\,\textsc{ii} regions.

Given the star formation history inferred by S17, we expect that at least some massive stars (conventionally those with $m_i \geq 8.0\,M_\odot$)

have already exploded as type II Supernova (SNII). We use the fraction of the total mass contributed by massive stars in the stellar mass ranges 8.0–40 $M_\odot$ and 40–100 $M_\odot$, computed by Romano et al. (2005) for several different initial mass functions (IMFs; Salpeter 1955; Tinsley 1980; Scalo 1986, 1998; Kroupa, Tout & Gilmore 1993; Chabrier 2003), to estimate the quantity of SNe exploded in SECCO 1, adopting $M_\star = 1.0 \times 10^5\,M_\odot$ from Table 1. The mass of stars with $m = 8$–40 $M_\odot$ ranges from a minimum of about 5500 $M_\odot$ with the IMF of Scalo (1986) to a maximum of $1.8 \times 10^4\,M_\odot$ with the IMF of Tinsley (1980). Stars in the range $m = 40$–100 $M_\odot$ contribute from about 300 $M_\odot$ (Tinsley 1980) to ~6000 $M_\odot$ (Chabrier 2003) to the total stellar mass budget of the system. Since, according to the Marigo et al. (2017) stellar models of the proper metallicity ($Z = 0.006$), the lifetime of a 40 $M_\odot$ star is $\simeq 5.0$ Myr and that of an 8 $M_\odot$ star is $\simeq 40.0$ Myr, we can conclude that, if the IMF of SECCO 1 is comprised within the range of cases considered here and independently of the detailed star formation history, several SNII explosions should have occurred in this system. Is this consistent with the fact that we do not see signatures of shocks in the spectra of the ionized regions of SECCO 1? Considering that in the spiral galaxy M33, Asvarov (2014) computed a number of about 1000 expected *alive* (i.e. observable) SNRs, we can just scale that number by the stellar mass ratios of the two galaxies (~10^{-4}), to roughly estimate the number of expected SNRs in SECCO1, obtaining only 0.1 SNRs. This number is indeed compatible with the non-detection of SNRs in our observations.

3.1 Kinematics, metallicity, and ionization of the diffuse gas

In Figs 2 and 3, we show the Hα velocity map (left-hand panel) and velocity dispersion map (right-hand panel), corrected for the intrinsic instrumental broadening for MB and SB, respectively. The maps show only the spaxels with $S/N > 3$ in the Hα line, whose parameters are derived by fitting a single Gaussian to every spaxel.
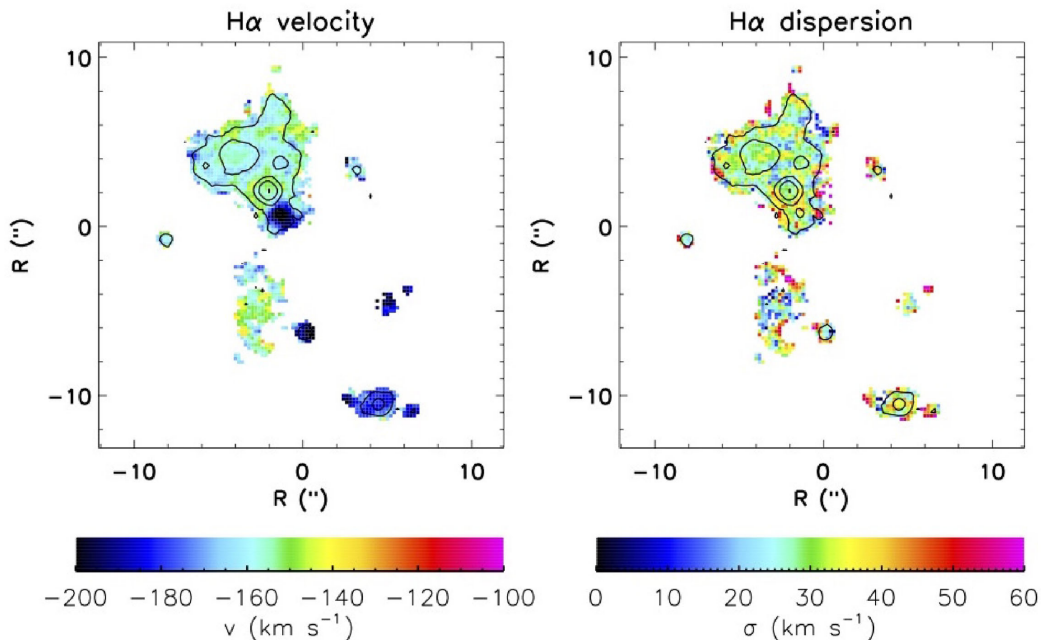

Figure 2. Kinematic maps for the Main Body. The Hα velocity (left-hand panel) and velocity dispersion (right-hand panel) are shown for all the spaxels with $S/N > 3$ after a Gaussian kernel smoothing of 3 pixels (0.6 arcsec). Hα contours are overplotted for reference, corresponding to 0.3, 0.8, 2, and 6 erg s^{-1} cm^{-2} Å^{-1}, respectively.
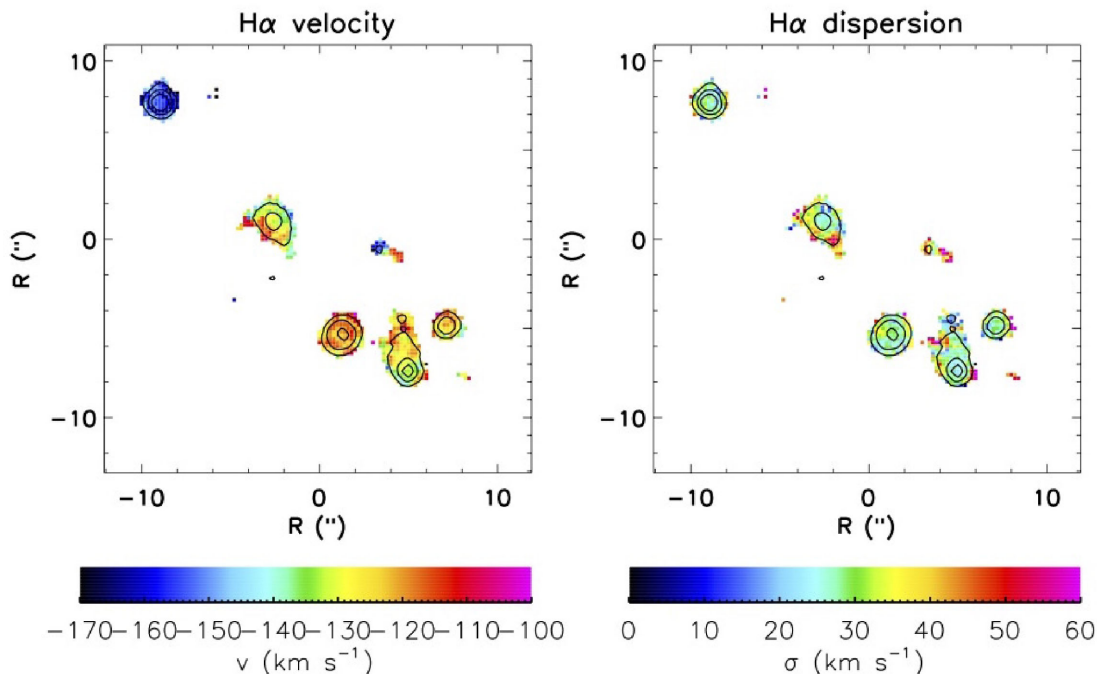
Figure 3. Kinematic maps and Hα contours for the Secondary Body. The arrangement and the meaning of the symbols are the same as in Fig. 2.

This view is complementary to the analysis of the individual H II regions presented in Be17a, as it traces also the properties of diffuse ionized gas that is present in SECCO 1. Not surprisingly, the systemic velocity of the diffuse gas follows the same velocity field as individual sources. The velocity dispersion of the gas within the nebulae (not shown in Be17a) is very uniform over the body of the system, with mean values typical of H II regions.

As discussed in Be17a (and already noted in B15b), some of the sources (in particular MB25, MB59, and MB61) show much stronger [O III] emission than the others (specifically, higher [O III]/Hβ ratios). This may be due to a different metallicity or to a different degree of ionization. To investigate the actual origin of the anomalous [O III] emission in these regions, we use the diagnostic diagram proposed by Dopita et al. (2016, D16 hereafter), which provides an estimate of both the ionization parameter U and the oxygen abundance 12+log(O/H) from a combination of rest-frame optical strong line ratios.

The D16 diagram is shown in the left-hand panel of Fig. 4, where the different grids show the variation of metallicity and log U for different values of ISM pressure. The spaxels with S/N > 3.0 in all the lines involved ([O III], Hα, Hβ, [N II] and [S II] doublet) are shown as points on the grid, coloured according to their positions in the diagram (outliers in log U in blue, spaxels in the high-metallicity tail in magenta, those in the low-metallicity tail in green, and all the others in black). The position of the blue, green, and magenta spaxels is superposed to the Hα emission map in the right-hand panel of Fig. 4. The high-ionization blue points are all clustered at the position of the sources with the anomalously high [O III] emission, strongly suggesting that the larger [O III]/Hβ ratio is not due to variation in metallicity, but to a higher ionization parameter at these locations. The spaxels tracing metallicities lower than 12+log(O/H) < 8.25 (green points) appear to correspond to diffuse gas between the detected H II regions, where the mixing of metals diffused by stellar winds and supernova explosions within each nebula is probably less effective. In any case, the metallicity variations are ±0.25

dex across the whole system, comparable to the uncertainties. Finally, if we limit the analysis to the spaxels with S/N > 5.0 in all the involved lines, *all* the magenta dots and most of the green ones (in particular, *all* those having 12+log(O/H) ≤ 8.06) disappear, showing that the tails of the metallicity distribution are populated by the noisier spaxels.[6] The high degree of chemical homogeneity of the system found in Be17a is confirmed using metallicity estimates from the D16 diagram. Fully analogous conclusions hold for SB. We do not show the D16 diagram for SB because in that piece of SECCO 1 there is no source displaying an anomalously high [O III] emission.

3.2 Spectroscopic constraints on the age of the youngest stellar population

To ionize an H II region, we need O or B stars. Dors et al. (2017) found that most extragalactic H II regions are ionized by stars in the T_{eff} range 37–40 kK, with an average value of 38.5 kK, corresponding to an MS lifetime shorter than 4 Myr (Pecaut & Mamajek 2013). This suggests that also in SECCO 1 the ionizing stars can belong to a very young population that may be difficult to unambiguously identify and characterize in a sparsely populated CMD. Note that 4 Myr is the age of the youngest isochrone in the PARSEC[7] set (Marigo et al. 2017) that we use in Section 4. To investigate this issue, we attempt to constrain the temperature and, consequently, the age of the stars powering the H II nebulae in SECCO 1, using our MUSE spectra.

---

[6] Note that in Be17a the contributions of all the spaxels associated with a given source were integrated together, providing source spectra with much higher S/N and, consequently, more robust metallicity estimates for the individual H II regions.
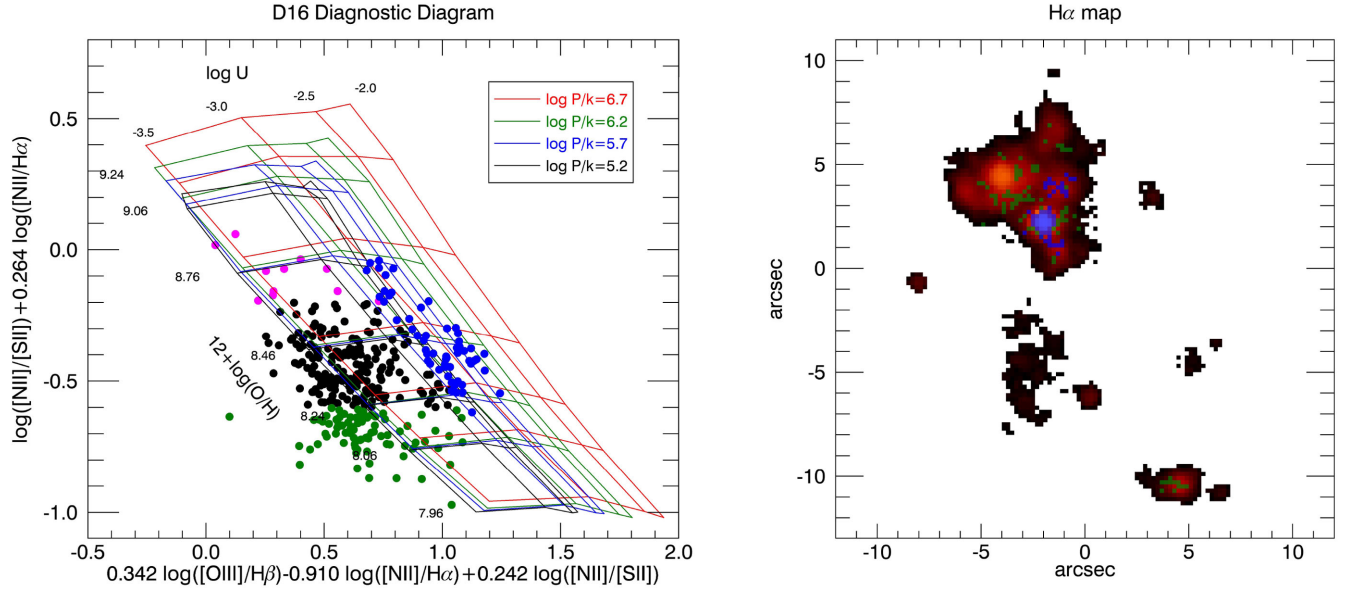
[7] http://stev.oapd.inaf.it/cgi-bin/cmd

Figure 4. The spatially resolved emission line diagnostic by Dopita et al. (2016) for spaxels in the SECCO Main Body with S/N>3.0 in all the emission lines involved. The diagnostic diagram is shown in the left-hand panel, where each point corresponds to a MUSE spaxel. The metallicity scale (increasing towards the upper part of the plot) and ionization parameter scale (increasing towards the right part) are shown on the different grids, corresponding to different values of the ISM pressure. The spaxels whose metallicity in the Dopita et al. (2016) scale is $12 + \log(O/H) < 8.25$ are plotted as green filled circles, those with $12 + \log(O/H) > 8.6$ as magenta filled circles, while the spaxels with $\log U > -3.0$ are shown as blue filled circles, independently of their oxygen abundance. The same spaxels are overplotted with the same colour code on the Hα map in the right-hand panel.

Table 2. Temperature and spectral type of ionizing stars.

Name unit	He I 5786 erg cm^{-2} s^{-1}	Hβ erg cm^{-2} s^{-1}	$\frac{HeI}{H\beta}$	T_{eff} K	ST^a
MB25	7.1 ± 1.7E-18	1.07 ± 0.02E-16	0.07 ± 0.02	$35\,000 \pm 2000$	O7.5V
MB26	8.1 ± 2.3E-18	5.00 ± 0.02E-17	0.16 ± 0.05	$53\,000 \pm 17\,000^{b,\,c}$	O2V
MB27	1.1 ± 2.6E-17	9.13 ± 0.02E-17	0.12 ± 0.03	$40\,000 \pm 3000$	O5.5V
MB30	9.5 ± 2.1E-18	6.86 ± 0.02E-17	0.14 ± 0.04	$47\,000 \pm 10\,000^{c}$	O2V
MB56	9.3 ± 2.2E-18	8.00 ± 0.02E-17	0.12 ± 0.03	$40\,000 \pm 3000$	O5.5V
MB61	1.2 ± 0.2E-17	8.65 ± 0.02E-17	0.14 ± 0.03	$42\,000 \pm 2000$	O4V
SB2	5.2 ± 1.6E-18	6.21 ± 0.02E-17	0.08 ± 0.03	$36\,000 \pm 2000$	O7V
SB45	5.4 ± 1.8E-18	6.08 ± 0.02E-17	0.09 ± 0.03	$37\,000 \pm 3000$	O6.5V

Notes. ^{a}Spectral types are from Pecaut & Mamajek (2013) for $T_{\text{eff}} \leq 46\,000$ K, while we associate the spectral type O2V to stars with $T_{\text{eff}} > 46\,000$ K.
$^b T_{\text{eff}}$ of this star is extrapolated from the relation given in fig. 9 of Kennicutt et al. (2000, lower continuous curve), since the relation is valid only for $T_{\text{eff}} < 50\,000$.
^{c}The large errors on the T_{eff} for these stars are due to the flattening of the relation between $\frac{\text{He I}}{\text{H}\beta}$ and T_{eff} for $\frac{\text{He I}}{\text{H}\beta} > 0.12$.

The effective temperature (T_{eff}) of the ionizing stars of a nearby H II region can be estimated through direct observation and spectral classification (see e.g. Walborn et al. 2014; Evans et al. 2015; Lamb et al. 2015). For more distant stars, we have an indirect estimate of T_{eff} based on the analysis of the emission lines of the nebular gas as proposed originally by Zanstra (1931) and later by Osterbrock & Ferland (2006). In particular, we have used the ratio between the He I 5876 Å line and Hβ which gives an estimate of the effective temperature nearly independent of the ionizing parameters (see e.g. fig. 9 of Kennicutt et al. 2000).

In Table 2, we summarize our results for all the Be17a H II regions where the He I line can be reliably measured from our MUSE data. In Fig. 5, we show the relevant portion of the MUSE spectrum for a representative sample of the sources listed in Table 2. The table reports the observed fluxes of the Hβ and of the He I lines, their ratios, the corresponding T_{eff}, and an indicative spectral classification.

All stars belong to the O spectral type, being all hotter than >35 kK. This means that they are more massive than 20 M$_\odot$ and indeed younger than $\simeq 4$ Myr. The main conclusion is that star formation occurred very recently in SECCO 1, in fact it may be currently ongoing.

4 *HST* +MUSE: THE STELLAR CONTENT OF SECCO 1

Using synthetic CMDs from stellar models, S17 concluded that the CMD they obtained from *HST* data is compatible with continuous star formation between 50 and 7 Myr ago. They found no evidence of older stars associated with SECCO 1 in their CMD and they established that the observed diffuse light can be accounted for by the unresolved low-mass counterpart of the 7–50 Myr old population. Unfortunately, the actual upper limit that S17 were able to put on the
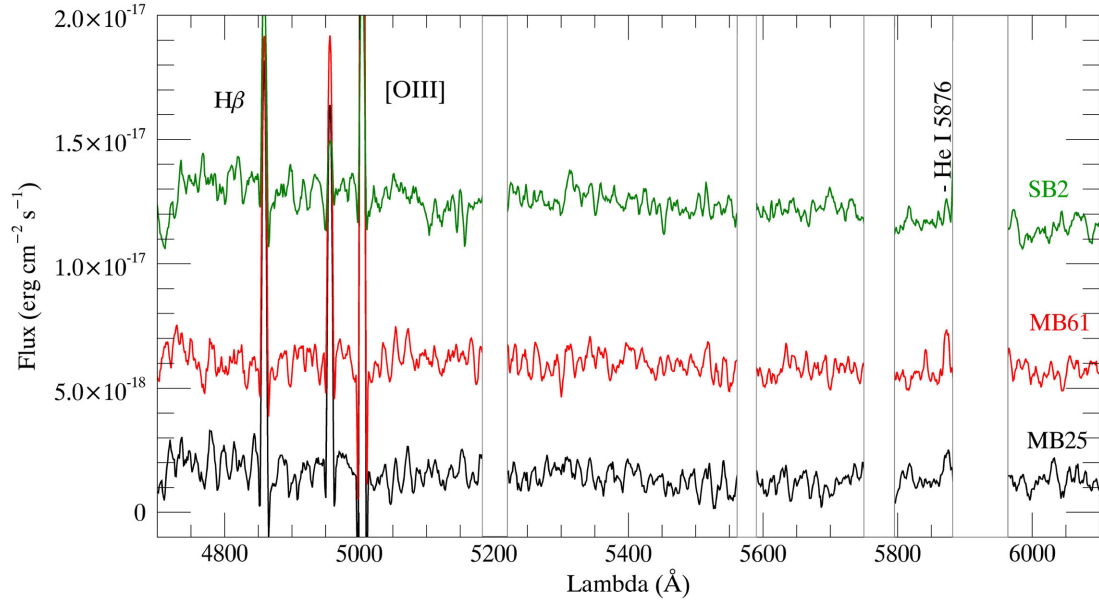
Figure 5. MUSE spectra (from Be17a) of three H II regions listed in Table 2, a representative of the quality of the whole sample (in terms of flux in the He I 5786 line). The spectra of the sources with the highest and the lowest He I 5786 fluxes (MB61 and SB2, respectively) are plotted, as well as an intermediate case (MB25). The spectral range shown includes the lines used to estimate the temperature of the ionizing stars. Arbitrary shifts in flux are applied to the spectra of MB61 and SB2 to make the plot readable. Blank vertical bands mask regions of the spectra badly affected by the residual of strong sky lines.

total mass in old stars is very weak, $M_\star < 6 \times 10^5$ M$_\odot$, i.e. the data are still compatible with the presence of an old stellar population comparable to or even larger than the young component, in mass.

Here, we re-analyse the stellar content of SECCO 1 in the light of the results obtained with MUSE, using the independent photometry we obtained from the S17 data, as described in Section 2.1. In Fig. 6, we show the CMD of four circular regions of the ACS-WFC field with a radius = 20 arcsec, corresponding to $\simeq 1.6$ kpc at $D = 17.0$ Mpc. The first two regions are centred on SECCO 1 MB and SB, respectively. The third is centred on a dwarf spheroidal galaxy (dSph) lying in the Virgo cluster that was serendipitously included in the ACS-WFC images of SECCO 1, Dw J122147+132853 after S17.[8] The fourth region samples a portion of the field far away from any resolved stellar system, as a Control Field (CF) providing an idea of the properties of the back/foreground population that should contaminate the CMDs of SECCO 1.

The CMD of the CF seems populated by the typical intra cluster (IC) population of Virgo, consisting of a Red Giant Branch (RGB; stars with age $\gtrsim$1–2 Gyr), and a broad vertical blue plume of unresolved background galaxies (see e.g. Williams, Ciardullo & Durrell 2007, and discussion and references therein). We used the deep CMD of Virgo IC stars by Williams et al. (2007) to derive the mean locus of background galaxies (plotted here as a thick vertical segment) and the thick polygonal contour approximately enclosing the IC RGB population near the RGB Tip. Note that, according to Williams et al. (2007), the IC RGB stars in their sample span the metallicity range $-2.3 \leq$ [M/H] ≤ 0.0. The limiting magnitude of our photometry is a strong function of colour and runs nearly

parallel to the right-hand side of the polygonal contour. Hence, the reddest stars of the IC RGB population are not seen here because they are beyond our detection limit. This implies that a population of metal-rich ($Z \gtrsim 0.004$) RGB stars associated with SECCO 1 may have gone undetected because the photometry is too shallow.

On the other hand, it is easy to see that the RGB stars dominating the CMD of the Dw J122147+132853 dSph are, on average, bluer than their IC counterparts, suggesting that the mean metallicity of the dSph is lower than that of the old IC population in this specific line of sight. Note that the clear detection of the RGB Tip of Dw J122147+132853 around F814W∼27.0 allows us to unambiguously locate it at the distance of the Virgo cluster. Since the dSph appears to contain only old stars, its CMD can be considered as an additional CF for F814W<26.5.

The CMDs of both MB and SB show an obvious excess of blue stars (F606W−F814W<0.0) and of red stars brighter than F814W = 25.5 with respect to the dSph field and the CF. These stars are the characteristic population of SECCO 1, as witnessed also by the significant fraction of them being cross-identified with peaks of Hα emission found by Be17a in the MUSE images (blue circles). The identification of sources associated with H II regions in the CMD of Fig. 6 is an important development with respect to the analysis by S17, with implications on the interpretation of the diagram (see below). The position of the MUSE sources in the ACS image is illustrated in the upper panels of Fig. 7, while in the lower panels of the same figure we overplotted the Hα intensity contours. There are several interesting considerations regarding the CMDs of Fig. 6:

(i) We confirm the conclusion by Be16, Be17a, and S17 that no trace of an excess RGB population is seen around SECCO 1. Unfortunately, the GO-13735 images are so shallow that only the very tip of the RGB of metal-poor/intermediate populations at $D \simeq 17.0$ Mpc can be (barely) reached, while the tip of metal-rich populations is below the detection threshold. Deeper photometry would allow us to draw much firmer conclusions on this crucial

[8] In the left-hand panel of fig. 14 by Be16 Dw J122147+132853 can be seen $\simeq 110$ arcsec to the West of SECCO 1 SB. It looks similar to other small LSB Virgo dwarfs identified in that paper but we do not include it in the Be16 list because it is partially superimposed on a distant disc galaxy, making its classification ambiguous.
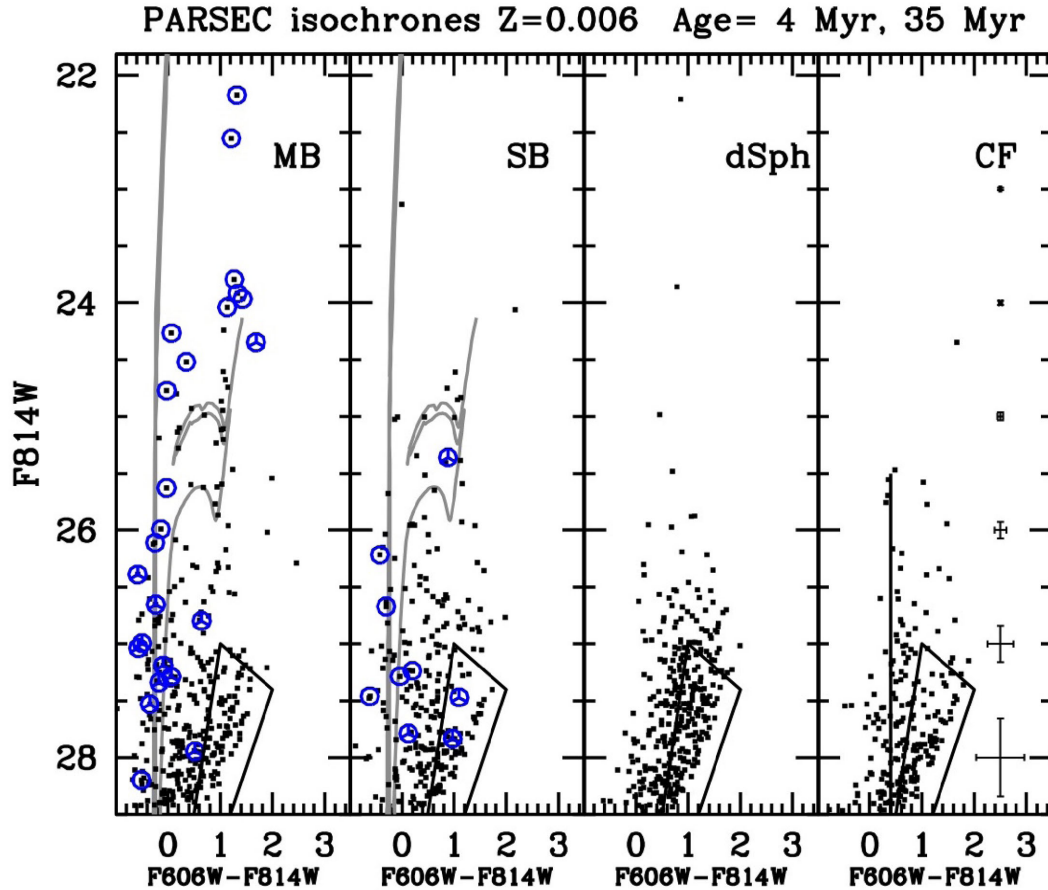
Figure 6. Colour–magnitude diagrams from *HST*/ACS photometry of circular regions of a radius = 20 arcsec centred, from left to right, on the centre of the main body of SECCO 1, on the centre of the secondary body of SECCO 1, on the centre of the Virgo dwarf spheroidal Dw J122147+132853, and on a region devoid of resolved stellar systems (CF). The polygonal contour at F814W ≤ 27.0 and F606W−F814W ≃ 1.0 approximately encloses the intra cluster population of RGB stars as sampled by Williams et al. (2007), the thick vertical segment at F606W−F814W = 0.4 is the ridge line of the blue population from the same source [the difference in $E(B-V)$ between the two lines of sights is <0.03 mag and it has been neglected]. Blue circles are sources cross-identified in the list of H II regions in Be17a; those having a skeletal triangle inscribed are recognized as more extended than individual point-sources by DOLPHOT. To superpose the PARSEC isochrones (grey curves), we adopted $D = 17$ Mpc and $E(B-V) = 0.048$.

issue. However, based on lack of detection also in diffuse light (S17), in the following, as a working hypothesis, we will assume that the star formation in SECCO 1 started ≲50 Myr ago.

(ii) The apparent lack of an RGB associated with SECCO 1 prevents a robust estimate of the distance of the system, which remains quite uncertain. For example, a distance as large as $D = 30$ Mpc, as unlikely as it may appear, cannot be firmly excluded with the existing photometric data. The luminosity of the O stars associated with the H II regions broadly implies $D \gtrsim 10$ Mpc (see Section 3.2). The strong deviation from the Hubble flow at distances larger than $\simeq 3$ Mpc (see e.g. McConnachie 2012) remains the most robust argument for SECCO 1 to belong to the Virgo cluster (see B15b) and to the LVC, in particular (S15, Be17a, S17).

(iii) We tentatively fit the CMD of SECCO 1 with two isochrones from the most recent PARSEC set (Marigo et al. 2017), with the mean metallicity of SECCO 1, as measured by Be17a, assuming $D = 17.0$ Mpc. The isochrones of age 4 Myr (light grey) and 35 Myr (dark grey) appear to nicely bracket the stellar population that can be unambiguously associated with SECCO 1. The comparison with the dSph and CF CMDs suggests that there is no compelling evidence for a significant population older than ≃35 Myr (but see S17).

We confirm that there is no obvious difference in stellar population between MB and SB (S17).

(iv) Reines et al. (2010) showed that the spectrum of the ionized gas can strongly affect the broad-band photometry of massive stars within H II regions. Both the continuum and strong emission lines can have a sizeable impact (note, e.g. that the F606W passband fully encloses both the [O III] and Hα lines, which are seen to vary by a considerable amount from region to region in SECCO 1, see Be17a). Hence, interpreting the position in the CMD of stars associated with H II regions (large blue circles in Fig. 6) with stellar isochrones may lead to misleading conclusions. This kind of effect is likely at the origin of the fact that some stars associated with H II regions have colours $F606W - F814W \sim 1.0$, typical of stars with $T_{\rm eff} \sim 4000$ K, while the observed nebular spectra require an ionizing source of much higher temperature ($T_{\rm eff} \gtrsim 30\,000$ K, see Section 3.2). Since some contribution from nebular spectra may affect also the stars not directly associated with an Hα peak detected in the MUSE data cubes (due to, e.g. diffuse emission, see Fig. 7), the overall CMD of SECCO 1 must be interpreted with some caution.

(v) We have marked with a skeletal triangle symbol the MUSE sources that are recognized by DOLPHOT as significantly more
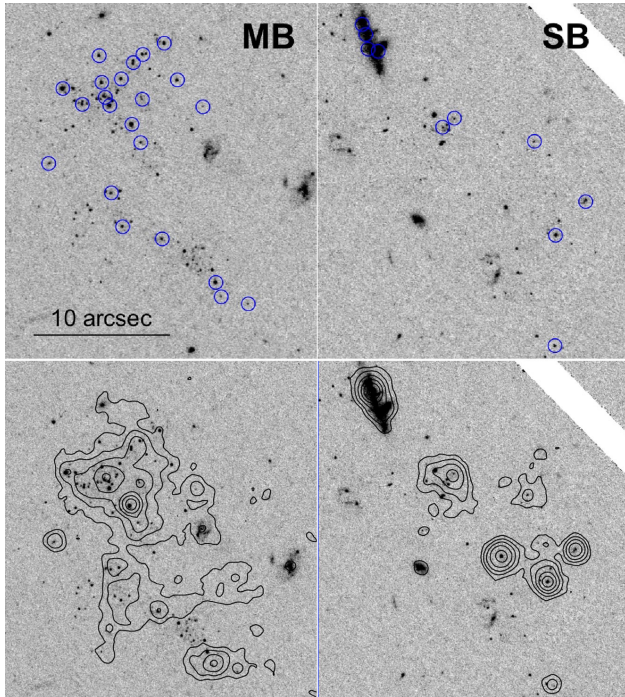
Figure 7. Upper panels: Hα emitting sources from Be17a having a counterpart in our catalogue from *HST* photometry are plotted as blue circles over two portions of the F606W ACS image of SECCO 1-MB (left-hand panel) and of SECCO 1-SB (right-hand panel). Lower panels: Hα intensity contours overplotted on the same image, with the same scale. The contour levels are from the outermost to the innermost: 0.5, 1.0, 2.0, 4.0, 8.0, and 16.0×10^{-18} erg cm^2 s^{-1}. In all the panels, North is up and East is to the left.

extended than point sources of the same magnitude, according to the sharpness parameter. Most of them are fainter than F814W = 26.5 while most of the brightest MUSE sources appear as normal stars. This implies that, in general, sources associated with H ɪɪ regions of SECCO 1 are unresolved in the available ACS images (i.e. are

point-like) and blending is the most likely reason why many of the faintest sources appear slightly extended.

5 Hα IMAGING: SEARCHING FOR ADDITIONAL PIECES

It is likely that some of the candidate Hα-emitting sources selected in Section 2.2 from the GTC images are not related to SECCO 1. Background galaxies that happen to have strong emission in the wavelength window of the f657/35 filter are an obvious example. Since SECCO 1 sources are clearly seen also in *GALEX* NUV images from the G ɪɪ survey, we decided to validate our candidates by asking that they are detected also in these images. Indeed, we found a source with strong Hα excess that is detected in the *GALEX* NUV image enclosing SECCO 1, $\simeq 3.3$ arcmin to the East–North–East of SB, as shown in Fig. 8. The source (ID number 100038 in our catalogue) is seen as extended both in the OSIRIS images and in the deep *g,r* images of the original SECCO survey (Bellazzini et al. 2015a). It has a nearby point-like companion (100046) with significant Hα excess. Despite the lack of a *GALEX* counterpart, we also include this source in the list of candidate additional H ɪɪ regions possibly associated with SECCO 1 (Table 3) because of its extreme proximity to 100038 (12.7 arcsec).

We derived a rough estimate of the Hα flux of 100038 and 100046 by comparison with SECCO 1 SB sources that have been measured in Be17a, assuming that the newly found candidates lie at the same distance. The derived fluxes are similar to those of confirmed SECCO 1 sources (Be17a). It is important to note that 100038 and 100046 lie just beyond the circle of a radius 4.0 arcmin centred on the centre of the OSIRIS field of view that is safe from any contamination of other interference orders and should be considered as the actual operative field of view of OSIRIS tunable filters. Moreover, all the known SECCO 1 sources that are seen in the OSIRIS images are not detected or very weak in the continuum images, while the continuum flux of the two candidates identified here is clearly detected. Still, especially given the *GALEX* detection of 100038, they remain good candidate H ɪɪ regions.
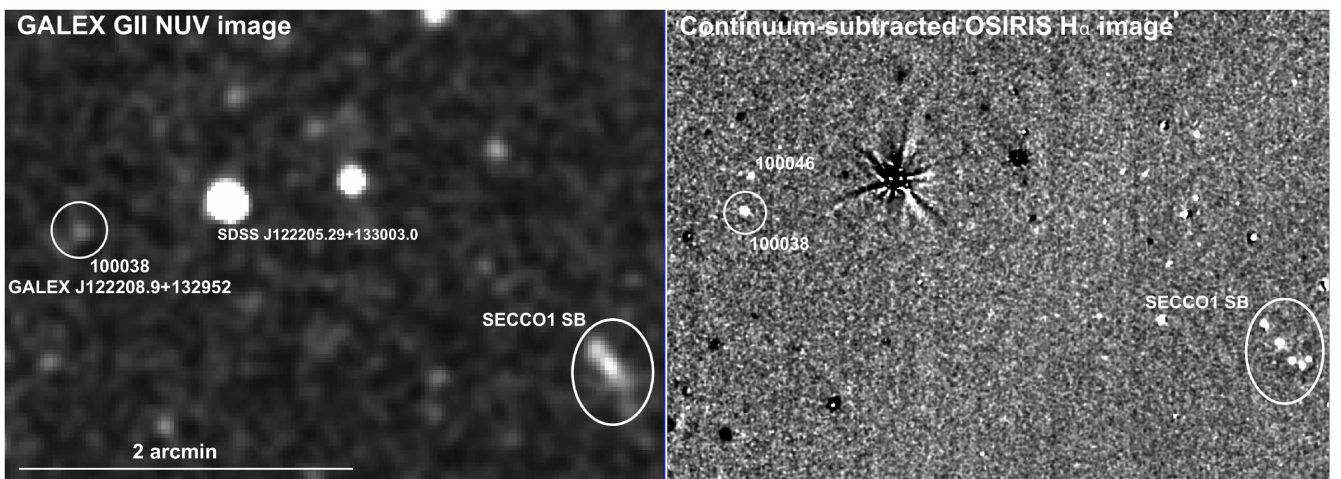

Figure 8. The newly identified candidate Hα emitter in the surroundings of SECCO 1. Left-hand panel: *GALEX* NUV image (with a Gaussian smoothing of 3 px size applied) with the source (100038/*GALEX* J122208.9+132962) labelled. A nearby bright star is also identified for reference, as well as SECCO 1 SB. Right-hand panel: continuum-subtracted Hα image from our GTC-OSIRIS observations. In addition to 100038 and SB, here we labelled the possible companion source 100046. Note that there are sources (outside SB) that have a significant residual in the Hα image but have no counterpart at all in *GALEX* (and vice versa). In both images, North is up and East is to the left.

Table 3. Additional candidate H II regions possibly associated with SECCO 1.

ID	*GALEX* ID	RA$_{J2000}$ deg	Dec.$_{J2000}$ deg	mag$_{NUV}$ mag	g^a mag	r^a mag	Hα flux^b 10^{-18} erg cm^{-2} s^{-1}
100038	J122208.9+132952	185.5373356	13.4980710	23.64 ± 0.42	22.430 ± 0.076	22.133 ± 0.041	≃ 210
100046		185.5365535	13.5015474		23.543 ± 0.087	22.994 ± 0.008	≃ 140

Notes. ^{a}Sextractor Kron magnitudes (`MAG_AUTO`) from the deep images of Bellazzini et al. (2015a).
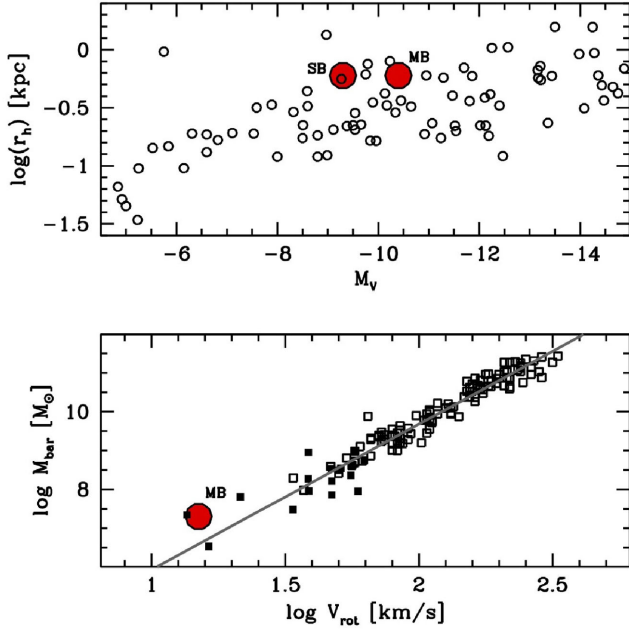^{b}Assuming the same distance of SECCO 1, $D = 17.0$ Mpc.

Figure 9. Upper panel: SECCO 1 MB and SB (large red filled circles) in the integrated absolute V magnitude versus log of the half-light radius diagram. Small empty circles are dwarf galaxies in the Local Group from McConnachie (2012). As a proxy for the half-light radius for MB and SB, we adopted half of the radial size reported (and defined) in Table 1. Lower panel: baryonic Tully–Fisher relation. Open squares are from Lelli et al. (2016) and filled squares are from Iorio et al. (2017); the grey line is the best fit for the accurate distances sample by Lelli et al. (2016). The baryonic mass of SECCO 1 MB (large red filled circle) has been computed by summing the H I mass corrected for the contribution of helium to the total gas mass according to Lelli et al. (2016); the rotation velocity is from A15, who provide an estimate of this quantity only for MB.

While a spectroscopic follow up is needed to ascertain the nature of 100038 and 100046, as well as other Hα sources lacking a *GALEX* counterpart, the overall result of our search for additional star-forming regions associated with SECCO 1 is largely negative. In particular, we did not find any reliable candidate in the region suggested by Be16 as possibly hosting additional SECCO 1 sources (see their fig. 14; the region is partially vignetted by the gap between the two chips of OSIRIS). The operative OSIRIS field samples a projected circular area with a radius ≃ 20 kpc around SECCO 1 at the distance of $D = 17$ Mpc, still only one candidate with properties analogous to known SECCO 1 pieces has been found.

6 THE NATURE OF SECCO 1

In Fig. 9, we show SECCO 1 MB and SB in the M_V versus log(r_h) relation for dwarf galaxies in the Local Volume (from McConnachie 2012) and in the baryonic Tully–Fisher relation (see Taylor et al.
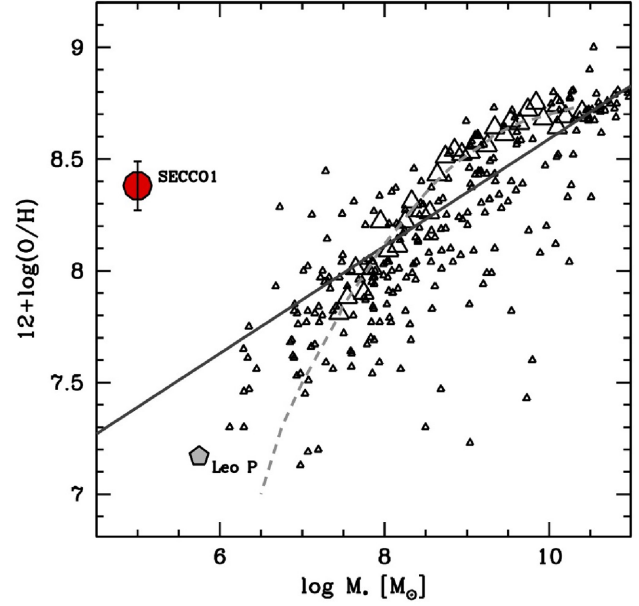

Figure 10. SECCO 1 as a whole into the stellar mass–metallicity relation. Small triangles are the $z \simeq 0$ sample of Hunt et l. (2016), large triangles are from Andrews & Martini (2013), and the light grey long-dashed curve is the best fit to the same data (from direct-method oxygen abundance estimates) extrapolated to low masses, from the same source. The dark grey continuous line is the stellar mass–metallicity relation from planetary nebulae by Gonçalves et al. (2014). SECCO 1 is represented as a large red filled circle.

2013; Lelli, McGaugh & Schombert 2016; Iorio et al. 2017, and references therein). Only MB is included in the last diagram since only for this component A15 provide an estimate of V_{rot} based on the velocity gradient seen in H I (see also Be17a). The two diagrams show that, taking the observables at face value, the structural and dynamical properties of SECCO 1 are in the range of those expected for a dwarf galaxy of the same baryonic mass.

On the other hand, the velocity field of the overall system (gas + stars), and the off-set in position between SB and AGC 229490 suggest that it is unlikely that the system is in dynamical equilibrium (see also Section 7, below). If confirmed, also the lack of an underlying old population would argue against the hypothesis that SECCO 1 is an ordinary, albeit very dark, dwarf galaxy (see Bekki 2015, for a theoretical framework for the evolution of almost-dark galaxies similar to SECCO 1).

However, the strongest, and likely ultimate, argument against this hypothesis is provided by Fig. 10, which displays how far SECCO 1 is from the stellar mass–metallicity relation of normal galaxies (see B15a, Be17a, S17). It is clear that such a high (and extremely homogeneous) metallicity cannot arise from chemical evolution within a stellar system of such low mass. The stripping of some pre-enriched gas from, e.g. the disc of a spiral galaxy appears as

the most likely origin for the system, as it would fit both the high metallicity and the (possible) lack of an old stellar population. There is no obvious way of distinguishing between a tidal stripping or a ram-pressure stripping event for the origin of SECCO 1. Indeed, as noted by Be17a, the location of SECCO 1 in Fig. 10 is typical of tidal galaxies (see e.g. Duc et al. 2014; Sweet et al. 2014, and references therein). However, star-forming knots similar to SECCO 1 are sometimes seen to originate in ram-pressure stripping episodes within galaxy clusters (*fireballs*, see e.g. Fumagalli et al. 2011; Yoshida et al. 2012; Kenney et al. 2014, references and discussion therein) and are predicted to occur in hydrodynamical simulations (Kapferer et al. 2009).

6.1 Comparison with fireballs

Yoshida et al. (2012), Hester et al. (2010), Fumagalli et al. (2011), and Kenney et al. (2014) provide very detailed analyses of star-forming knots within Hα tails likely arising from strong ram-pressure stripping events in galaxy clusters. All these authors refer to these compact UV and Hα emitting blobs as *fireballs*. The similarities of SECCO 1 with fireballs were already briefly noted in B15a; here, we make a more thorough comparison.

Yoshida et al. (2012) show that fireballs have emission line ratios typical of H II regions and the same metallicity as the gas in the parent galaxy. They have typical sizes similar to SECCO 1 (1–2 kpc, but with $r_h \simeq 200$–300 pc) and similar or larger stellar masses (e.g. those considered by Fumagalli et al. 2011, have 3.9×10^4 M$_\odot \leq M_\star \leq 5.0 \times 10^5$ M$_\odot$). Typical mean ages seem larger than SECCO 1, in the range ~ 80–400 Myr, but $(g - r)$ colours are similar to SECCO 1 and the presence of H II regions implies very recent/ongoing star formation. Fumagalli et al. (2011) report a star formation rate of 10^{-3}–10^{-4} M$_\odot$yr^{-1}, again pretty similar to SECCO 1. Kenney et al. (2014) report on the detection of a single unresolved H I cloud with a mass 3.7×10^7 M$_\odot$, not clearly associated with an individual fireball but having systemic velocity similar to several H II regions in the ram-pressure tail of IC 3418.

While many intrinsic properties of fireballs are quite similar to those of SECCO 1, there is also at least one remarkable difference. Fireballs are found within a few tens of kpc from their parent galaxy, within obvious cometary tail structures, and they ignited the star formation as soon as they were stripped. On the other hand, the cloud that formed SECCO 1 travelled for a long time away from its parent galaxy and it is currently forming star in conditions of extreme isolation.

6.2 Candidate parent galaxies

Be17a proposed the interacting galaxy pair formed by NGC 4299 ($V_h = +258$ km s^{-1}) and NGC 4294 ($V_h = +369$ km s^{-1}) (Chung et al. 2009) as a possible site of origin for the gas cloud that is now SECCO 1.[9] The gas distribution of these galaxies shows signs of the effects of both ram pressure and tides and their velocities are compatible with the range of LVC galaxies, but they are more than 500 kpc apart from SECCO 1, in projection (see Table 1). S17 noted that the M 86 ($V_h = -183$ km s^{-1}) group is also a member of the Virgo LVC and it is located at $\simeq 350$ kpc, in projection, from SECCO 1. Galaxy–galaxy interactions are clearly ongoing and, in particular, M 86 is likely interacting with NGC 4438 ($V_h = +98$ km s^{-1}) and
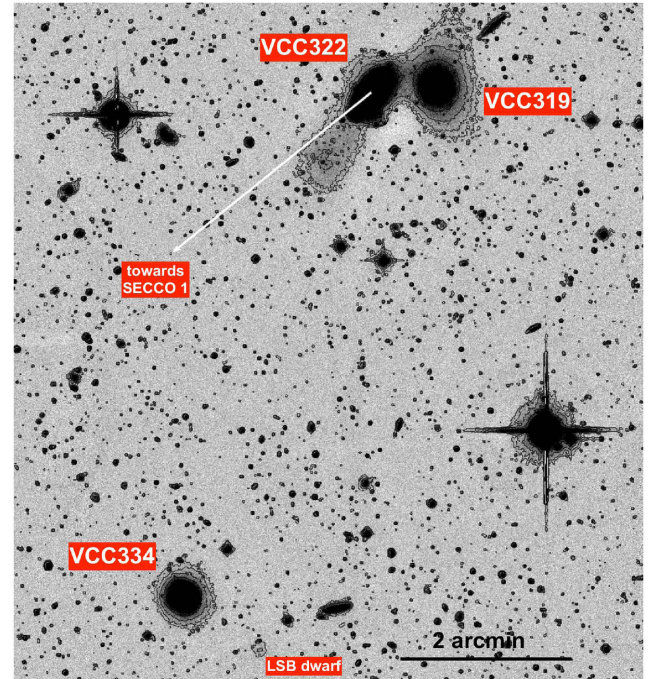

Figure 11. Deep *g*-band image of the interacting group of dwarfs suggested as a candidate site of origin of SECCO 1, from the Next Generation Virgo cluster Survey (Ferrarese et al. 2012). North is up and East is to the left. Density contours at arbitrary intensity levels have been drawn to put in evidence low surface brightness substructures, like the prominent tidal tail of VCC 322 or the very low SB dwarf to the West–South–West of VCC 334 (labelled). The white arrow shows the direction from VCC 322 towards SECCO 1 MB.

both seem to be undergoing ram-pressure stripping, with a short X-ray and Hα emitting tail generically pointing in the direction of SECCO 1. We note that in the surroundings of the same group an extended H I tail is probably being stripped from NGC 4388 ($V_h = +2555$ km s^{-1}) by its interaction with M 86 in a direction nearly perpendicular to that towards SECCO 1 (Oosterloo & van Gorkom 2005), showing that this environment is particularly active as a source of stripped H I clouds.

In Fig. 11, we present a new promising candidate site for the origin of SECCO 1, the group of dwarf galaxies VCC 322 ($V_h = -438$ km s^{-1}), VCC 319 ($V_h = -209$ km s^{-1}), and VCC 334 ($V_h = -213$ km s^{-1}).[10] These have velocities typical of LVC members and are likely mutually bound and interacting. Two of them are gas-rich and star forming (VCC 322 and VCC 334) while the other is red and with no H I detected. Their absolute integrated *r* magnitudes are all enclosed between $M_r = -15.9$ and -16.1. The stellar masses, derived as in Bellazzini et al. (2017) adopting the colour versus mass-to-light relations by Roediger & Courteau (2015), are $M_\star \simeq 9.0 \times 10^7$ M$_\odot$, 3.8×10^8 M$_\odot$, and 8.3×10^7 M$_\odot$ for VCC 322, VCC 319, and VCC 334, respectively. In projected distance, they are closer to SECCO 1 than the candidates described above ($\simeq 250$ kpc, see Table 1).

However, the feature that makes them particularly promising as candidate parents for SECCO 1 is their chemical composition. Both VCC 322 and VCC 334 have good spectra in the range

---

[9] All the parameters of candidate parent galaxies reported in this section are taken from the SIMBAD data base, http://simbad.u-strasbg.fr.

[10] The NGSV image shown in Fig. 11 reveals the presence of a very low surface brightness amorphous galaxy located $\simeq 70$ arcsec to the West–South–West of VCC 334. This may be an additional member of the group.

Table 4. Initial parameters of the simulation: hot gas temperature T_{hot}, hot gas density n_{hot}, hot gas metallicity Z_{hot}, cloud temperature T_{cl}, cloud density n_{cl}, cloud metallicity Z_{cl}, cloud radius R_{cl}, and cloud velocity v_{cl}.

T_{hot} (K)	n_{hot} (cm^{-3})	Z_{hot} ($Z_\odot$)	T_{cl} (K)	n_{cl} (cm^{-3})	Z_{cl} ($Z_\odot$)	R_{cl} (kpc)	M_{cl} ($M_\odot$)	v_{cl} (km s^{-1})
5×10^6	2.5×10^{-5}	0.1	5×10^3	2.6×10^{-2}	0.5	3.7	9.4×10^7	200

3800 Å $\lesssim \lambda \lesssim$ 9200 Å from the Sloan Digital Sky Survey – Data Release 12 (Alams et al. 2015) with measured fluxes for several strong emission lines.[11] We estimated the oxygen abundance of these two galaxies in the same way as we did for SECCO 1 in Be17a, averaging the results of the indicators N2 and O3N2 from Pettini & Pagel (2004). For both galaxies, we obtain 12 + log(O/H) = 8.3 ± 0.2, i.e. the same abundance of SECCO 1, within the uncertainties (that here include observational errors and uncertainties in the calibrations of the relations between oxygen abundances and strong-line indicators), and consistent with the range of abundances of galaxies with that stellar mass, albeit slightly on the high side, possibly suggesting that they indeed lost some mass in the past. Adopting the linear stellar mass–metallicity relation by Gonçalves et al. (2014), shown in Fig. 10, 12 + log(O/H) = 8.10, 8.09, and 8.25 is obtained for VCC 322, VCC 334, and VCC 319, respectively.

A close two/three-body encounter may have produced the required stripping episode. It is tantalizing to imagine that the same episode transformed VCC 319 into the passive gas-less system that we see today.

7 HYDRODYNAMICAL SIMULATIONS OF A PRESSURE-SUPPORTED CLOUD

Be17a estimated that if the gas cloud that gave rise to SECCO 1 detached from the interacting galaxy pair NGC 4299 + NGC 4294, it should have travelled for at least ∼1.2 Gyr within the LVC ICM to reach its current position, given the projected distance to the pair and the radial velocity difference. Analogous computations imply travel times $\gtrsim$ 1.0 Gyr also from the other proposed parent galaxies or galaxy groups. Hence, the extreme isolation of SECCO 1 implies that the system has survived within its environment for a long time before the onset of star formation. Is this occurrence realistic? Are such kinds of clouds expected to have lifetimes longer than 1 Gyr? To attempt an answer to the last question, we performed a two-dimensional high-resolution hydrodynamical simulation of a cold gas cloud travelling through a hot and low-density ambient medium, with the typical features of the LVC ICM.

7.1 Simulation set-up

The simulation was carried out with the ATHENA code (Stone et al. 2008), using a two-dimensional Cartesian geometry and a fixed grid with size 40 kpc × 40 kpc and spatial resolution 5 pc × 5 pc. We included a module for the classical thermal conduction (Spitzer 1956) with an efficiency of 10 per cent (accounting for the presence of tangled magnetic fields) and a module for radiative gas cooling and heating in the presence of collisional ionization, and photoionization from a uniform UV background at redshift $z = 0$.

---

[11] See dr12.sdss.org/spectrumDetail?plateid=1766&mjd=53468&fibre=56 and http://dr12.sdss.org/spectrumDetail?plateid=1766&mjd=53468&fibre=50 for VCC 322 and VCC 334, respectively.

Cooling and heating rates have been obtained through the CLOUDY spectral synthesis code (Ferland et al. 2013) and the spectrum of the background radiation field has been taken from Haardt & Madau (2012). The temperature cut-off for radiative cooling is 10^3 K, then molecular cooling is not included in our simulation. For further details on the hydrodynamical treatment of thermal physics, we refer to Armillotta, Fraternali & Marinacci (2016) and Armillotta et al. (2017). Moreover, we used an adaptive and moving grid that follows the cloud during its own motion. We neglected the presence of an external gravitational potential and self-gravity inside the cloud (we justify the latter assumption in Section 7.2).

The parameters of the simulation are listed in Table 4. The temperature of the hot gas, $T_{hot} = 5 \times 10^6$ K, was calculated through the following formula:

$$T_{hot} = \frac{3\sigma_r^2 \mu_{hot} m_p}{2k_B},$$ (1)

where $\mu_{hot} \simeq 0.59$ is the mean molecular weight of the hot gas, m_p the proton mass, k_B the Boltzmann constant, and $\sigma_r \sim 208$ km s^{-1} is the radial velocity dispersion of the ICM in LVC (Boselli et al. 2014). The hot gas metallicity was set to 0.1 $Z_\odot$, according to the metallicity of the ICM at 1.1 Mpc from the centre of the Virgo cluster (Urban et al. 2011), where 1.1 Mpc is the projection on the sky of the physical distance between NGC4216, the central galaxy of LVC, and M87, the central galaxy of Cluster A. Finally, the numerical density of hot gas was set to 2.5×10^{-5} cm^{-3}. This value was derived from the total mass (dark and baryonic matter) density in LVC. For this calculation, we assumed that the hot gas density distribution follows the dark matter density profile given by Navarro, Frenk & White (1996):

$$\rho(r) = \rho_{cr} \frac{\Delta_{vir}}{3} \frac{c_{vir}}{f(c_{vir})} \frac{r_s^3}{r(r + r_s)^2},$$ (2)

where ρ_{cr} is the critical density of the Universe and Δ_{vir} is the virial overdensity provided by the dissipationless spherical top-hat collapse. In the ΛCDM cosmological model with $\Omega_m = 0.3$, the value of Δ_{vir} is ∼340 at $z = 0$ (Bryan & Norman 1998). Moreover, c_{vir} is the concentration parameter associated with the mass, M_{vir}, contained within the virial radius, r_{vir}, $r_s \equiv r_{vir}/c_{vir}$ is a scale radius and $f(c_{vir})$ a function of c_{vir} (see Duffy et al. 2008, for definitions of c_{vir} and $f(c_{vir})$ at redshift $z = 0$). The virial mass of LVC, $M_{vir} \sim 1.2 \times 10^{13} M_\odot$, has been estimated through the virial theorem:

$$M_{vir} = \frac{3r_{vir}\sigma_r^2}{G},$$ (3)

where G is the gravitational constant and the virial radius, r_{vir}, is defined as the radius of a sphere within which the average mass density is $\Delta_{vir}\rho_{cr}$. By using equation (2), we calculated the total mass density, $\rho(r)$, at 430 kpc from the centre of LVC, where 430 kpc is the projection on the sky of the physical distance of SECCO 1 from the central galaxy of LVC. The mass density of hot gas was estimated by multiplying $\rho(r = 430$ kpc) by the universal baryon
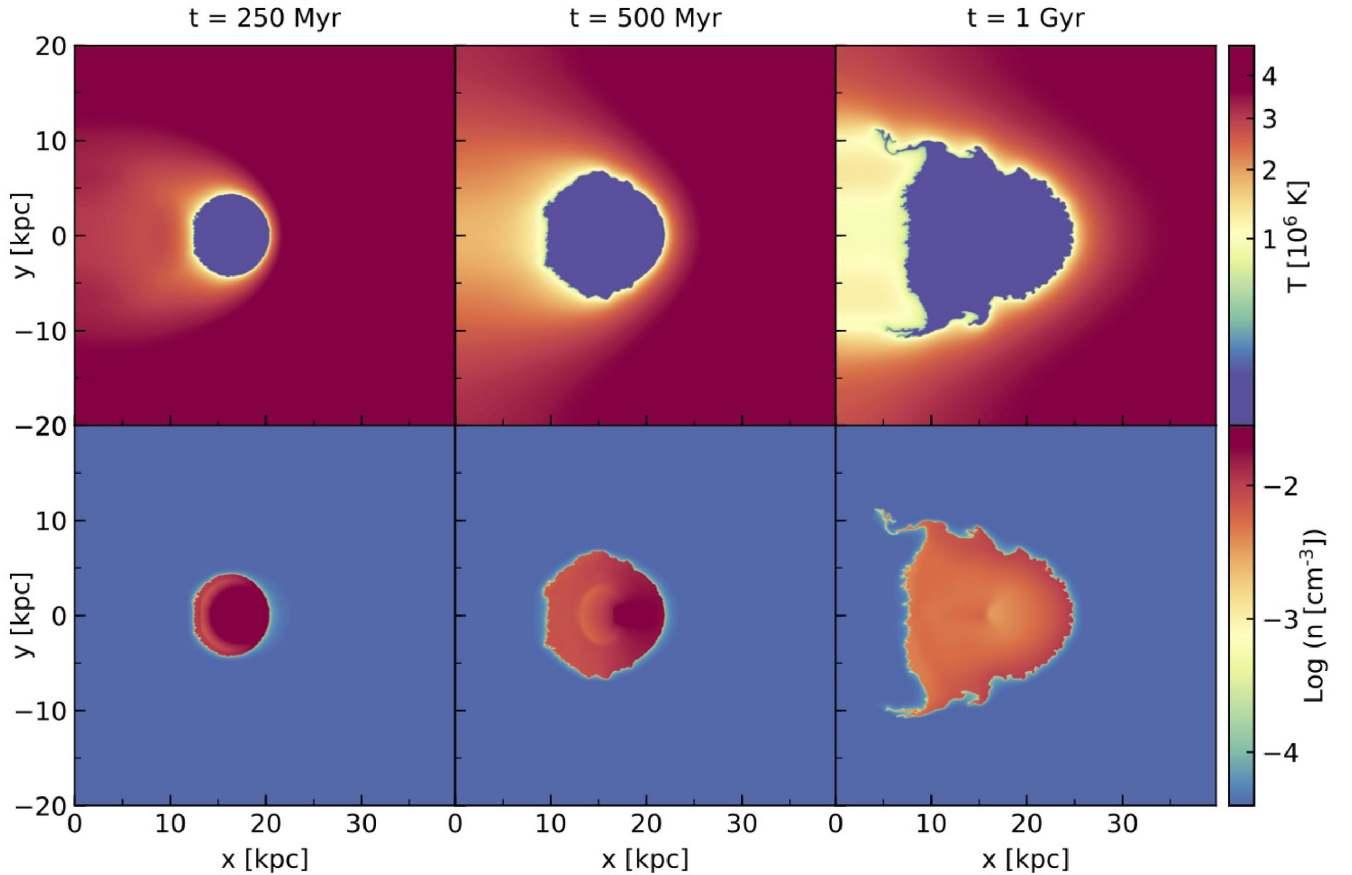
Figure 12. Temperature (top panels) and number density (bottom panels) snapshots of the simulation at $t = 250\,\mathrm{Myr}$ (left-hand panels), $t = 500\,\mathrm{Myr}$ (middle panels), and $t = 1\,\mathrm{Gyr}$ (right-hand panels) for the 2D simulation.

fraction ($\sim$0.17, e.g. Komatsu et al. 2009) by the expected fraction of hot gas ($\sim$0.3; Dai et al. 2010).

For the cloud temperature, we adopted a value of 5000 K, according to the mean temperature of the diffuse H I (e.g. Wolfire et al. 2003; Roy et al. 2013). The cloud metallicity was set to 0.5 $Z_\odot$, following Be17a. The cloud velocity with respect to the surrounding medium is set at 200 km s^{-1}, similar to the velocity dispersion of the LVC (Boselli et al. 2014). The cloud radius is 3.7 kpc (A15). We note that the cloud is fully resolved since its radius is almost three orders of magnitude larger than the resolution of our spatial grid. From the radius and the total H I mass, we derived the H I numerical density of the cloud, $n_{\mathrm{cl,HI}} \simeq 2.9 \times 10^{-3}$ cm^{-3}. To calculate the total numerical density, n_{cl}, we divided $n_{\mathrm{cl,HI}}$ by $\mu_{\mathrm{cl}} \simeq 0.71$, the mean molecular weight of the cloud, and $X_{\mathrm{HI}}/A \simeq 0.16$, the mass abundance of H I with respect to all elements at $T = 5000$ K and $Z = 0.5\,Z_\odot$. Both these values have been obtained through our CLOUDY modelling. We found $n_{\mathrm{cl}} \simeq 2.6 \times 10^{-2}$ cm^{-3}. We note that this value of density almost corresponds to the density required for the cloud to be in pressure equilibrium with the ambient medium. Given this density and including the contribution of neutral and ionized hydrogen, helium and metals, the total mass of the cloud is $M_{\mathrm{cl}} = 9.4 \times 10^7\,\mathrm{M}_\odot$. The simulation ran for 1 Gyr.

7.2 Results

Figs 12 and 13 display the results of our simulation. Fig. 12 shows the temperature (top panel) and number density (bottom panel)
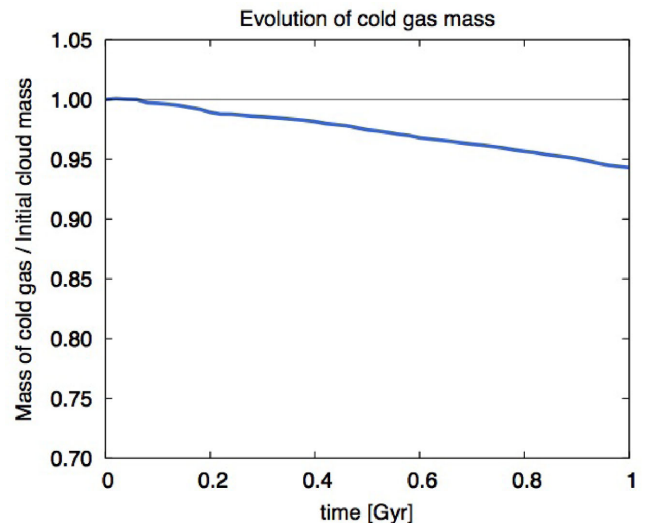

Figure 13. Evolution of the cold gas ($T < 2 \times 10^4$ K) fraction as a function of time in the 2D simulation.

distributions on the grid at different simulation times. The cloud evolution proceeds quite slowly during 1 Gyr. Until 250 Myr, the initial spherical cloud is completely intact, and all its features (temperature, density, and radius) remain nearly constant. The only difference is the presence of a parabolic layer around the cloud,

characterized by temperatures that slowly increase from the cloud to the ambient temperature. This effect is explained by the presence of thermal conduction, which smooths the temperature gradients at the interface between cold and hot gas, leading the gas cloud to evaporate. After 250 Myr, hydrodynamical instabilities start to develop at the edge of the cloud, slowly causing its deformation. Moreover, the cloud expands – with an average radius that increases by more than a factor of 2 after 1 Gyr – decreasing its density but keeping its temperature nearly constant. Indeed, in order to preserve pressure equilibrium with the ambient medium, the cloud continuously adapts to the surrounding thermodynamical changes. The gas temperature around the cloud decreases both because thermal conduction makes the temperature gradient more and more smooth, and because the gas lost from the cloud quickly evaporates creating a wake at intermediate temperature. As a consequence, the cloud density decreases, while its temperature remains constant due to thermal effects, as we discuss later.

Fig. 13 shows the time evolution of the mass of cold gas at $T < 2 \times 10^4$ K. Above such a temperature, the hydrogen is generally completely ionized. The loss of cold gas mass from the cloud is negligible, it is ~ 6 per cent of the initial mass of the cloud after 1 Gyr.

The cloud survival strongly depends on the efficiency of ram pressure exerted by the ambient medium. External ram pressure slows down the cloud during its motion, triggering the formation of hydrodynamical instabilities and the subsequent cloud destruction. However, the efficiency of ram pressure decreases with increasing the cloud mass. The time-scale associated with this phenomenon is the so-called drag time (e.g. Fraternali & Binney 2006):

$$t_{\mathrm{drag}} = \frac{M_{\mathrm{cl}}}{v_{\mathrm{cl}} \sigma \rho_{\mathrm{hot}}} , \qquad (4)$$

where $\sigma \simeq \pi R_{\mathrm{cl}}^2$ is the cross-section of the cloud. In our case, $t_{\mathrm{drag}} \sim 28$ Gyr, more than two orders of magnitude larger than the simulation time. The relatively large mass of the cloud and the low density of the surrounding medium make the ram-pressure effect very weak and justify its solid body-like behaviour. The low density of the medium is justified by the fact that the cloud is located at the edges of the LVC halo. Indeed, the distance of the cloud from the centre of LVC, 430 kpc, is slightly larger than the virial radius, ~ 400 kpc (see equation 3).

The cloud is also stabilized by thermal effects. According to our CLOUDY cooling function, $T \sim 6000$ K is the equilibrium temperature between radiative cooling and heating at numerical density $n \sim n_{\mathrm{cl}}$. Moreover, the cloud evaporation driven by thermal conduction is very slow. According to the classical theory, the evaporation time of our cloud is ~ 24 Gyr (Cowie & McKee 1977, where we considered an efficiency of thermal conduction of 10 per cent), once again two orders of magnitude larger than the simulation time.

In order to evaluate if the presence of self-gravity could affect our results, we calculated the virial ratio of the cloud. The virial ratio is a dimensionless value that measures the gravitational binding of a cloud: clouds with the virial ratio lower than 2 are gravitationally bound. For our cloud, the virial ratio is ~ 4, *indicating that the cloud is pressure-supported and globally stable against the collapse*. The main effect that the presence of self-gravity could have on the global evolution of the cloud should be to further stabilize it against the formation of hydrodynamical instabilities (Murray et al. 1993).

Given all the above considerations, we can conclude that gas clouds similar to SECCO 1 can be long-lived in the LVC environment and can travel nearly intact for hundreds of kpc from the site of their formation (see also Burkhart & Loeb 2016). The results of

the *N*-body/hydrodynamical simulations by Kapferer et al. (2009, discussed in more detail below) also suggest that cold gas clouds can be long-lived in the cluster medium, as ram-pressure stripped gas clumps are still alive at the end of their simulation, 0.5 Gyr after the stripping event. It is also interesting to note that the friction of the ICM has only minor effects. The systemic velocity of the cloud decreases by just $\simeq 8.0$ km s^{-1} in the 1 Gyr of our simulation.

7.3 A lower resolution simulation in three dimensions

As an independent validation of the results of our 2D simulation, we ran a lower resolution, three-dimensional hydrodynamic simulation of a cold gas cloud flowing in a hot medium, adopting a very similar set-up. We used a customized version of the grid-based, Adaptive Mesh Refinement (AMR) hydro-code RAMSES (Teyssier 2002). In our three-dimensional Cartesian Grid, the computational box has a volume of $L_{\mathrm{box}}^3 = (40 \, \mathrm{kpc})^3$. Since a resolution similar to that of the 2D simulation is computationally prohibitive, we run a small series of 3D simulations at increasing resolutions, starting from the same initial conditions, and checked numerical convergence in order to assess the robustness of our results.

Another difference with respect to the 2D set-up concerns the grid, which in this case is not fixed. We exploit instead the reduced computational cost of the AMR technique. Initially, the refinement criterion is geometry-based: maximum resolution[12] is assigned to a sphere of size ~ 8 kpc, chosen to be larger than the whole cloud. The resulting initial grid is nested, with the computational region located outside the maximum resolution sphere refined at intermediate resolution; the minimum resolution, ~ 2.5 kpc, is adopted in the outermost regions of the box. At later times, the refinement strategy is discontinuity-based, i.e. resolution is increased in regions presenting a steep density contrast.

As initial conditions, in a reference frame whose origin is placed at the centre of the cold gas cloud, the hot gas is moving along the *x*-axis at a velocity of 200 km s^{-1}. The cold cloud is assumed to be homogeneous and characterized by a uniform temperature, as the external, hotter medium, representing the ICM. The initial parameters characterizing both the cloud and the ICM are the same as the ones used in the 2D simulation (Table 4).

Also in this case, radiative cooling and heating are taken into account. The cooling function implemented in RAMSES takes into account both atomic (i.e. due to H and He) and metal cooling (see Few et al. 2014). The contribution from metals at temperatures above 10^4 K is accounted for through a fit of the difference between the cooling rates calculated at solar metallicity and those at zero metallicity using the photoionization code CLOUDY (Ferland et al. 1998). At lower temperatures, metal fine-structure cooling rates are from Rosen & Bregman (1995). The effects of a UV background are also taken into account. The RAMSES cooling routine includes functional fits for the photoheating and photoionization rates of the Haardt & Madau (1996) ionizing background spectrum, as formulated in Theuns et al. (1998). The adopted normalization of the UV flux and the slope of the spectrum are the same as used for the 2D simulation. The minimum temperature is set to $T_{\mathrm{min}} = 5000$ K. In our 3D simulations, we do not take into account thermal conduction.

Two-dimensional density and temperature maps of the 3D simulations are shown in Fig. 14 at the same time-steps displayed in Fig. 12 for the 2D simulation, to ease a direct comparison. Each

---

[12] The maximum resolution can be computed as $L_{\mathrm{box}} \times 0.5^{levelmax} \sim 78$ pc, where $levelmax = 9$ is the maximum refinement level used in this work.
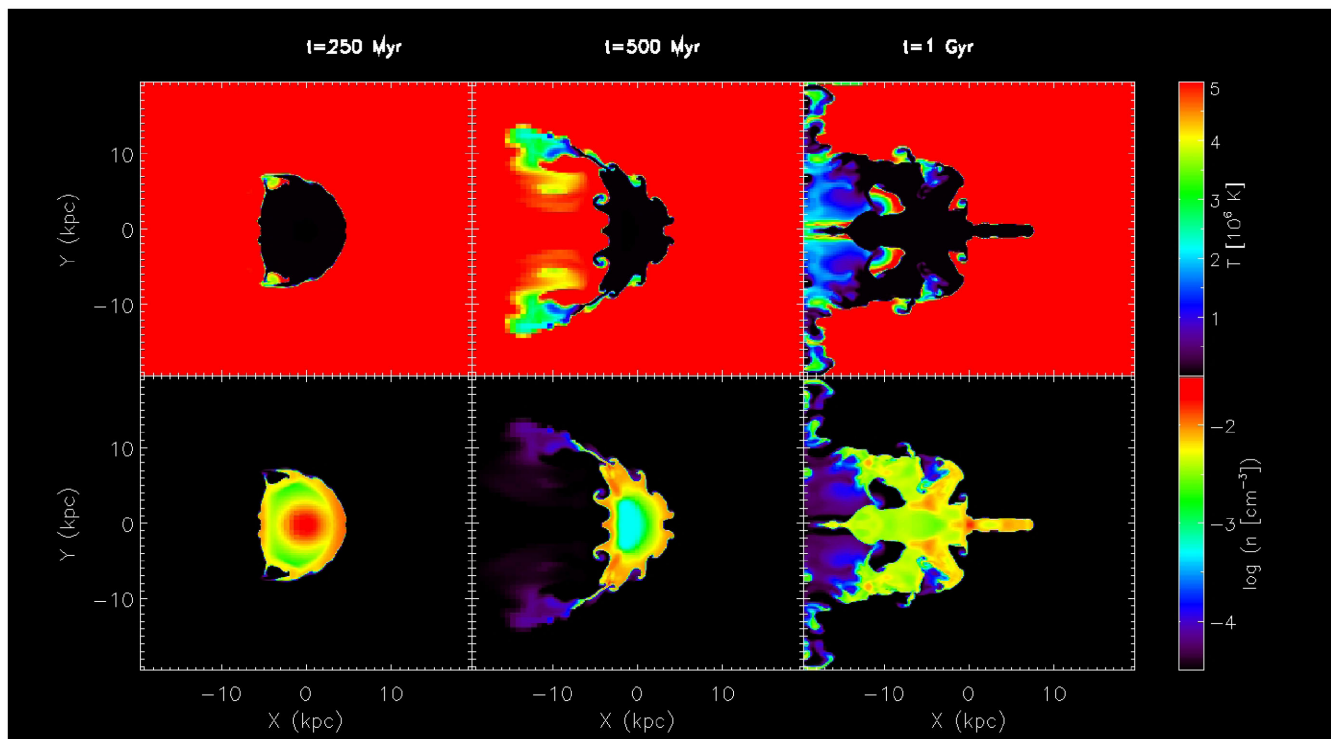
Figure 14. Temperature (top panels) and number density (bottom panels) snapshots of the simulation at $t = 250\,\text{Myr}$ (left-hand panels), $t = 500\,\text{Myr}$ (middle panels), and $t = 1\,\text{Gyr}$ (right-hand panels) for the 3D simulation.

map represents a section of the computational domain in the x–y plane.

The lack of thermal conduction makes the cloud much more prone to the effects of Kelvin–Helmholtz instabilities, leading to a faster evolution, with respect to the 2D simulation (as expected according to Armillotta et al. 2016), with significant morphological changes. Throughout the evolutionary time considered here, from the initially spherical shape, the cold cloud evolves into a typical umbrella-like or jellyfish-like shape, already seen in previous studies (e.g. Kwak, Henley & Shelton 2011; Marinacci et al. 2011; Scannapieco & Brüggen 2015).

At $t = 0.5\,\text{Gyr}$, the x–y cross-section of the cloud has significantly thinned. Cold gas is being continuously ablated from the cloud and mixed with the hotter ICM. As visible in the density and temperature maps, the material present at the upper and lower edges of the cloud appears stretched outwards. The thin, extended filaments driven by the shear instabilities cause the coolest gas to extend for nearly 20 kpc along the y-direction. As a consequence of such effects, the originally cold matter of the cloud undergoes a substantial re-distribution in that, besides being reduced to a thinner shell, the volume occupied by the cold gas also increases along the z-direction. This goes along with a strong decrease of the central density. At this time, the wake of the cloud is still tenuous ($n \leq 10^{-4}\,\text{cm}^{-3}$) and hot ($T \sim 10^{6.5}\,\text{K}$).

At $t = 1\,\text{Gyr}$, the turbulent mixing of the cold and hot layers in the wake has led to an increase of the filling factor of hot gas at $T \sim 10^6\,\text{K}$. Although the distribution of the coolest gas is still preserving a substantial degree of symmetry with respect to the x-axis, at this epoch its stretching is extreme. A prominent, elongated bar is visible in the front of the cloud, whereas the average density of the wake has globally increased. Similar protruding structures in the front of cold clouds moving fast in a very hot medium have been

found also in previous 2D (Kwak et al. 2011) and 3D (Scannapieco & Brüggen 2015) hydrodynamic studies, as well as the presence of a few cold cloudlets detaching from the wake.

However, Fig. 15 shows that, notwithstanding the considerable morphological evolution, a large fraction ($\simeq 75\,\text{per cent}$) of the original cold gas is preserved. Despite the notoriously greater difficulty in obtaining numerical convergence in AMR simulations than in uniform grid ones (e.g. Calura et al. 2015, and references therein), Fig. 15 also shows that the cold mass decrease is rather robust with respect to resolution.

Hence, the results of the 3D simulations confirm that under the conditions chosen in this work, after 1 Gyr the majority of the initial cloud mass is still cold. The 2D and 3D simulations lead to the same verdict, i.e. the considered gas cloud can survive a travel of 1 Gyr (corresponding to $\simeq 200\,\text{kpc}$ in our simulations) through an ambient mimicking the LVC, losing only between 5 and 25 per cent of the original cold gas. We also note that, convolving the end state of both simulations with the beam of the VLA data by A15, to simulate their observations, the resulting images are broadly compatible with the observed H I density maps presented by these authors.

8 STAR FORMATION IN STRIPPED CLOUDS

Having established that a compact pressure-supported cloud similar to SECCO 1 can probably survive >1 Gyr long journeys within the Virgo ICMs, it remains to be explored what may have triggered the onset of the current episode of star formation just a few tens of Myr ago.

In Fig. 16, we plot the gaseous components of MB and SB in the size–column density diagram, together with other H I clumps with or without detected star formation inside, following Burkhart & Loeb (2016). These authors observe that these pressure-supported
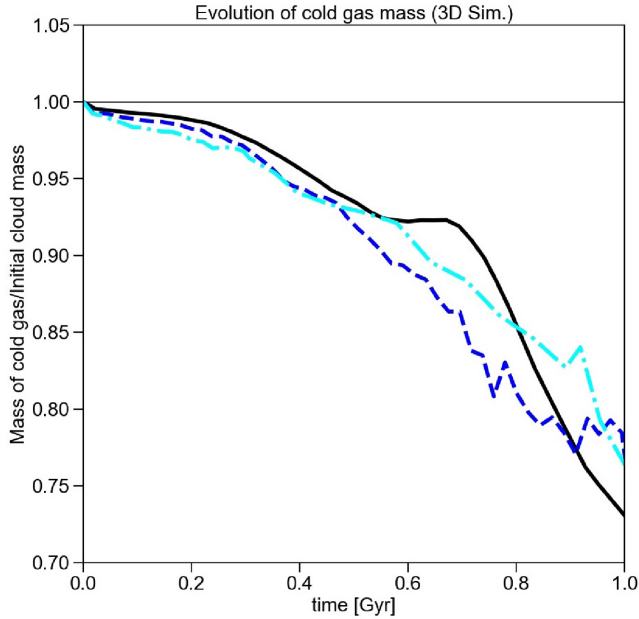
Figure 15. Evolution of the cold gas ($T < 2 \times 10^4$ K) fraction as a function of time in the 3D simulation. The results from simulations with three different values for the maximum resolution are shown, as a convergency test. Dot–dashed cyan line: *levelmax* = 7, dashed blue line: *levelmax* = 8, and black continuous line: *levelmax* = 9. The corresponding maximum resolution is 312 pc, 156 pc, and 78 pc, respectively.
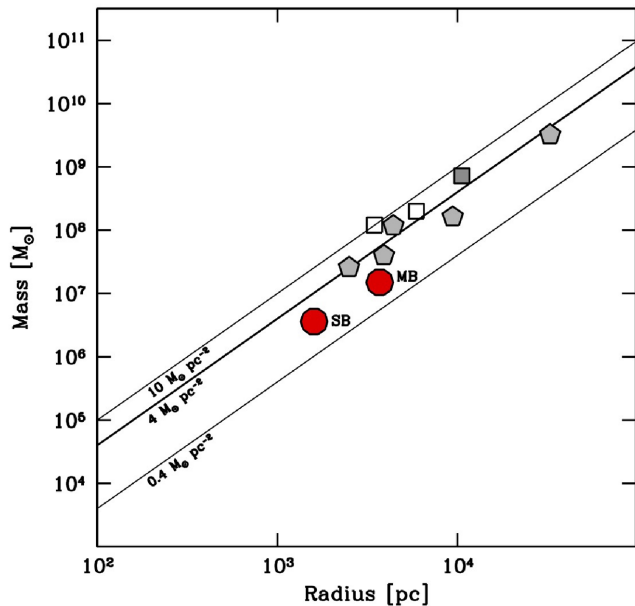

Figure 16. Size versus mass relationship for starless or nearly starless H I clouds, following Burkhart & Loeb (2016). Squares are from Janowiecki et al. (2015), pentagons from Cannon et al. (2015), grey filled symbols are clouds where star formation has been detected. SECCO 1 MB and SB are plotted as large red filled circles and labelled. Their H I radii and masses used in this plot are from A15. The lines are loci of constant column density, where 4–10 $M_\odot pc^{-2}$ is the range of critical the surface density for the formation of molecular hydrogen. Gas clouds should lie above these lines to be able to ignite star formation.

clouds are near the critical density threshold to form molecular hydrogen (4–10 $M_\odot pc^{-2}$) and, consequently, are likely on the verge of igniting star formation (indeed, some of them are already forming stars). They suggest that pressure fluctuations and tidal shear may drive the clouds to cross the critical density line, eventually triggering a star formation event.

We note that SECCO 1 MB and SB are not far from the other dark or almost-dark H I clouds plotted in Fig. 16 but lie below the generally accepted critical density lines. However, this may be due to the smearing effect of the VLA beam of A15 observations. The two gas clouds associated with SECCO 1 may be fragmented in smaller sub-clumps where the actual density is, in fact, above the threshold. The extreme isolation of SECCO 1 makes tidal shear unlikely to have triggered star formation in this case and it is unclear what can cause a significant pressure fluctuation in the surroundings of the system. Perhaps, during the travel, the density of the cloud may slowly increase, finally leading to the critical conditions to ignite star formation. This should be investigated with future simulations including self-gravity.

In this context, it is worth considering the relevant results of the thorough study by Kapferer et al. (2009). These authors performed *N*-body/hydrodynamical simulations, with radiative cooling, star formation, and stellar feedback, of the ram-pressure stripping of a large disc galaxy in a cluster environment. The final outcome of the simulations varies depending on the relative velocity of the galaxy and the ICM and on the density of the ICM, but, in general they find (a) that the gas stripped from the disc can reach distances of ≃400 kpc from the parent galaxy in just 500 Myr, (b) that star formation occurs at any time in the compact gas clouds that form in these extended ram-pressure wakes, and (c) that some of these clouds, at any distance from the parent galaxy along the wake, are still forming stars in the last 50 Myr of the 500 Myr-long simulation, and hence may host H II regions.[13] These long-lived star-forming knots are broadly comparable to SECCO 1.

However, there is a remarkable difference between the results presented by Kapferer et al. (2009) and the observations of SECCO 1. In all the simulations, the star-forming knots are part of a huge and structured wake including several dense gas clumps (with or without recent star formation) and an extended cometary tail of stars formed in the wake at any epoch. At odds with this scenario, the ALFALFA survey did not detect any additional UCHVC or H I structure (like, e.g. the one discussed by Oosterloo & van Gorkom 2005) in the surroundings of SECCO 1 (Adams et al. 2013).[14] Moreover, S17 searched for small star-forming knots similar to SECCO 1 on deep Next Generation Virgo cluster Survey (NGVS; Ferrarese et al. 2012) optical images, sampling a region of about 1.3 × 1.3 Mpc (in projection) around SECCO 1, finding only a few candidates that do not seem related to SECCO 1.

8.1 Candidate dark clouds in Virgo

It is worth noting that there are three additional UCHVCs from the Adams et al. (2013) sample that B15a searched for stellar counterparts (finding none) that (a) are projected on to the sky area covered

---

[13] Note, however, that all the star-forming knots that are active in the last 50 Myr in the Kapferer et al. (2009) simulations are associated with an underlying older population that is not observed in SECCO 1, at least within the limits of currently available *HST* and ground-based photometry.

[14] ALFALFA covers most of the extension of the Virgo cluster in the sky and its full velocity range, and it is sensitive down to ∼3.0 × 10⁷ $M_\odot$ at that distance (Hallenbeck et al. 2012; Huang et al. 2012).

by the Virgo cluster, (b) have systemic velocity within the range covered by Virgo galaxies, and (c) have physical properties, as seen by ALFALFA, very similar to the original cloud where we discovered SECCO 1 (HVC 274.68+74.0). These are HVC 277.25+65.14-140 (SECCO Field C), HVC 298.95+68.17+270 (Field M), and HVC 290.19+70.86+204 (Field X), see B15a and Be16. Adopting $D = 17.0$ Mpc and using equation (7) by Adams et al. (2013), we find that, if they are indeed located in the Virgo cluster, two of them (HVC 277.25+65.14-140 and HVC 290.19+70.86+204) have also H I masses very similar to HVC 274.68+74.0 (a few 10^7 M$_\odot$, on that scale), while HVC 298.95+68.17+270 would have $M_{\rm H\,I} \simeq 4 \times 10^8$ M$_\odot$. These are good candidates to be pressure-supported clouds like SECCO 1 in which star formation has not (yet?) started (see also Taylor et al. 2013, 2017; Burkhart & Loeb 2016, and references therein). Note, however, that they cannot be related to SECCO 1 since they are more than 1.5 Mpc away from it, in projection. It is also worth stressing that while a clustering of blue stars like SECCO 1 MB would have been easily identified by B15a or S15, a sparser group (e.g. smaller or more dispersed than SB) could be impossible to identify in broad-band optical/UV images. Deep Hα relatively wide-field imaging would be the only efficient way to exclude the presence of isolated H II regions or young stellar systems with $M_\star < 10^4$ M$_\odot$ within these clouds, whose typical projected size is ∼5 arcmin–10 arcmin (Adams et al. 2013).

Finally, we note that in both the UCHVC samples of Saul et al. (2012) and Adams et al. (2013), there are a few additional objects whose position in the sky and radial velocity are compatible with membership or association with the Virgo cluster.[15] Hence, it is quite possible that a small but non-negligible population of compact, dark and isolated pressure-confined H I clouds living in or around this cluster has been already observed.

9 SUMMARY AND CONCLUSIONS

We presented a thorough analysis and discussion of the available data on the almost-dark stellar system SECCO 1, with additional results from the MUSE observations shown in Be17a,b and an analysis of the stellar content of the system, based on coupling the stellar photometry from *HST*-ACS data and MUSE spectroscopic data. We also presented the results from deep Hα imaging of the surroundings of the system obtained with OSIRIS@GTC. By means of a set of dedicated 2D and 3D hydrodynamical simulations, we studied the evolution of a gas cloud mimicking SECCO 1. The main observational results can be summarized as follows:

(i) All the Hα emitting sources identified in SECCO 1 by Be17a are unequivocally classified as H II regions based on line ratio diagnostics. We do not see any trace of SNRs in our MUSE data. The velocity dispersion within ionized nebulae is similar to that generally observed in typical H II regions.

(ii) We provide evidence that the anomalously high [O III]/Hβ ratios observed in a few sources of SECCO 1 by Be17a are not due to differences in metallicity with the other sources but to differences in the ionization status. Hence, all the oxygen abundance estimates

of H II regions in SECCO 1 obtained in Be17a are reliable and robust.

(iii) Spectral line diagnostics suggest that the stars that are ionizing the gas in the H II regions should be very young (age$\lesssim$ 4 Myr).

(iv) The analysis of the CMD of SECCO 1 with the H II regions cross-identified implies that most of the star formation in SECCO 1 likely occurred within the last 35 Myr, with no perceivable sign of old or intermediate-age populations associated with the system. However, deeper photometry is required to completely rule out the presence of an old population, especially if it is as metal rich as the H II regions or more.

(v) The inconsistency between the broad-band colours of some stars associated with H II regions and the temperature of the ionizing sources estimated from nebular lines suggests that the position of these sources in the CMD is likely affected by the nebular spectrum, making the interpretation of the CMD less straightforward (see Reines et al. 2010).

(vi) By means of deep Hα imaging of a field of a projected radius $\simeq$ 20 kpc, we were able to identify only one robust candidate star-forming region (with a *GALEX* counterpart) possibly associated with SECCO 1, confirming the remarkable isolation of this system. A spectroscopic follow up is required to ascertain the actual nature of the candidate.

Based on the above points, on the numerical simulation presented here as well as on previous results from the literature, we can make some final considerations on the nature of SECCO 1:

(i) While the structural and kinematical parameters of SECCO 1, taken at face value, are consistent with fundamental scaling laws of galaxies (namely the M_V versus $\log(r_h)$ relation and the baryonic Tully–Fisher relation, see Section 6, for discussion), its oxygen abundance is a factor of $\gtrsim 10$ larger than the typical galaxy of the same stellar mass. This implies that the system most likely originated from a ram-pressure or tidal stripping event that removed a pre-enriched gas cloud from a galaxy with $M_\star \gtrsim 10^8$ M$_\odot$. The virial ratio of the gas cloud indicates that it is not gravitationally bound but it is confined by the external pressure.

(ii) The main physical properties of SECCO 1 are very similar to those of *fireballs* (Fumagalli et al. 2011; Yoshida et al. 2012). However, star formation is ignited in fireballs virtually as soon as the gas from which they form is stripped from the parent galaxy by ram pressure, while SECCO 1 is extremely isolated and star formation is currently ongoing.

(iii) We identified another possible site of origin for the stripped gas cloud that formed SECCO 1. It is an interacting triplet of dwarf galaxies (VCC 322, VCC 319, VCC 334) that is closer to SECCO 1 in projection than previously suggested candidates, and whose members have oxygen abundance very similar to SECCO 1.

(iv) Independently of the actual site of origin, the stripped gas cloud that formed SECCO 1 should have travelled for ∼1 Gyr within the ICM of LCV before the onset of the currently ongoing star formation episode (or, perhaps, forming stars more or less continuously, like some of the gas blobs in the simulations by Kapferer et al. 2009). The hydrodynamical simulations that we performed suggest that a pressure-supported gas cloud like SECCO 1 can probably survive such a long time in the considered environment, in agreement with previous results from the literature. The process that leads the cloud to cross the critical density to ignite star formation is unclear and cannot be investigated with the simulations presented here. The current unremarkable environment of SECCO 1 suggests some kind of slow internal mechanism as the most plausible driver of this density evolution.

---

[15] In particular, limiting to those lying in the range $180.0° \leq$ RA $\leq 195.0°$ and $0.0° \leq$ Dec. $\leq 20.0°$, HVC 292.94+70.42+159, HVC 295.19+72.63+225, in the Adams et al. (2013) list, and 183.0+04.4-112, 184.8+05.7-092, and 188.9+14.5+387, in the Saul et al. (2012) list. In the Saul et al. (2012) sample, we considered only clouds classified as *Candidate Galaxies* (CG).

(v) We note that three of the Adams et al. (2013) UCHVCs included in the SECCO survey are compatible with belonging to the Virgo cluster (or to one of its substructures). They are quite similar to SECCO 1 and, assuming a distance of $D = 17.0$ Mpc, also the H I mass of two of them is virtually the same as SECCO 1. Since B15a found no sign of stellar counterpart in their very deep images, they are good candidate pressure-supported gas clouds that have not yet ignited star formation (like those considered by Burkhart & Loeb 2016, see discussion and references therein). These clouds, if they are indeed located in Virgo, are just above the sensitivity limit of ALFALFA (in H I mass). Hence, they may be the tip of the iceberg of a large population of compact gas clouds floating in galaxy clusters (see S17 for further discussion). This hypothesis is supported by the fact that, in addition to those considered here, a handful of the UCHVCs identified by Saul et al. (2012) and Adams et al. (2013) also have positions and velocities compatible with association with the Virgo cluster.

One of the most remarkable features of SECCO 1 is that it comes in two pieces. There are only two possible paths to this outcome, in the very likely hypothesis that stripping is at the origin of the overall system. MB and SB were independently stripped from the same parent galaxy and/or fragmented during the stripping event, and managed to fly together for more than 1 Gyr. On the other hand, one can imagine that they were a single cloud that fragmented in two pieces, perhaps at the onset of the current star formation episode, due, e.g. to mechanical feedback from supernovae. If fragmentation occurred 35 Myr ago, the observed projected distance would imply a velocity difference of $\gtrsim 180 \, \mathrm{km \, s^{-1}}$.

Indeed, the effect of SN feedback on SECCO 1 is probably the most interesting issue to be studied, e.g. by means of numerical simulations, as it will not only help to clarify the origin of the system but also to understand its fate. Would the stars remain bound together as hypothesized by Yoshida et al. (2012) for the fireballs? Is the spatial offset between SB and the AGC 229490 cloud due to gas ejection by Supernova-driven winds or to the natural lag of the stars that are immune from the friction exerted by the ICM on the gas? But, if this is the case, why is the same offset not seen in MB? The two pieces should have similar direction of motion in the plane of the sky, hence the lag between stars and gas should be similar. The offset between SB and AGC 229490 implies velocities in the range ~ 50–$500 \, \mathrm{km \, s^{-1}}$ for ejection times between 35 and 4 Myr ago. Such velocities seem incompatible with a lag due to ram pressure, since, according to our simulation, in that time-scale it would have produced a negligible velocity difference between the gas and the stars ($< 1.0 \, \mathrm{km \, s^{-1}}$). Unfortunately, the uncertainties on the actual status of the medium in which SECCO 1 is immersed and the limitations of our simulations prevent us to draw firm conclusions from these kinds of arguments. It is also interesting to note that the total baryonic mass of SECCO 1 MB is above the threshold generally considered sufficient to retain SN ejecta (see e.g. Willman & Strader 2012, and references therein).

Finally, it can be speculated that even if SECCO 1 will be further fragmented into individual H II regions (or compact groups of them), once the ionizing sources have exploded as SNe, the stars of lower mass within individual regions may remain bound as star clusters with size $\lesssim 5$ pc and mass $\sim 10^2$–$10^4 \, \mathrm{M_\odot}$. If this is the case and SECCO 1 in not a unique system, *intra cluster open clusters* should be found free-floating in Virgo (and in other galaxy clusters as well), in addition to globular clusters (Tamura et al. 2006).

REFERENCES

Adams E. K., Giovanelli R., Haynes M. P., 2013, ApJ, 768, 77
Adams E. K. et al., 2015, A&A, 580, A134 (A15)
Alams S. et al., 2015, ApJS, 219, 12
Andrews B. H., Martini P., 2013, ApJ, 765, 140
Armillotta L., Fraternali F., Marinacci F., 2016, MNRAS, 462, 4157
Armillotta L., Fraternali F., Werk J. K., Prochaska J. X., Marinacci F., 2017, MNRAS, 470, 114
Asvarov A. I., 2014, A&A, 561, A70
Bacon R. et al., 2014, The Messenger, 157, 13
Beccari G., Bellazzini M., Battaglia G., Ibata R., Martin N., Testa V., Cignoni M., Correnti M., 2016, A&A, 591, 56 (Be16)
Beccari G. et al., 2017a, MNRAS, 465, 2189 (Be17a)
Beccari G. et al., 2017b, MNRAS, 468, 4254 (Be17b)
Bekki K., 2015, MNRAS, 454, L41
Bellazzini M., Perina S., Galleti S., Oosterloo T. A., 2011b, A&A, 533, A37
Bellazzini M. et al., 2015a, A&A, 575, 126 (B15a)
Bellazzini M. et al., 2015b, ApJ, 800, L15 (B15b)
Bellazzini M., Belokurov V., Magrini L., Fraternali F., Testa V., Beccari G., Marchetti A., Carini R., 2017, MNRAS, 467, 3751
Bertin E., Arnouts S., 1996, A&AS, 317, 393
Boselli A. et al., 2014, A&A, 570, A69
Bryan G. L., Norman M. L., 1998, ApJ, 495, 80
Burkhart B., Loeb A., 2016, ApJ, 824, L7
Calura F., Few C. G., Romano D., D'Ercole A., 2015, ApJ, 814, L14
Cannon J. M. et al., 2015, AJ, 149, 72
Chabrier G., 2003, PASP, 115, 763
Chung A., van Gorkom J. H., Kenney J. D. P., Crowl H., Vollmer B., 2009, AJ, 138, 1742

Cowie L. L., McKee C. F., 1977, ApJ, 211, 135
Dai X., Bregman J. N., Kochanek C. S., Rasia E., 2010, ApJ, 719, 119
Dolphin A. E., 2000, PASP, 112, 1383
Dopita M. A., Kewley L. J., Sutherland R. S., Nicholls D. C., 2016, Ap&SS, 361, 61 (D16)
Dors O. L., Hägele G. F., Cardaci M. V., Krabbe A. C., 2017, MNRAS, 466, 726
Duc P. A., Paudel S., McDermid R. M., Cuillandre J.-C., Serra P., Bournaud F., Cappellari M., Emsellem E., 2014, MNRAS, 440, 1458
Duffy A. R., Schaye J., Kay S. T., Dalla Vecchia C., 2008, MNRAS, 390, L64
Evans C. J. et al., 2015, A&A, 574, A13
Ferland G. J., Korista K. T., Verner D. A., Ferguson J. W., Kingdon J. B., Verner E. M., 1998, PASP, 110, 761
Ferland G. J. et al., 2013, RMxAA, 49, 137
Ferrarese L. et al., 2012, ApJS, 200, 4
Few C. G., Courty S., Gibson B. K., Michel-Dansac L., Calura F., 2014, MNRAS, 444, 3845
Fossati M., Fumagalli M., Boselli A., Gavazzi G., Sung M., Wilman D. J., 2016, MNRAS, 455, 2028
Fraternali F., Binney J. J., 2006, MNRAS, 366, 449
Fumagalli M., Gavazzi G., Scaramella R., Franzetti P., 2011, A&A, 528, A46
Fumagalli M., Fossati M., Hau G. K., Gavazzi G., Bower R., Sun M., Boselli A., 2014, MNRAS, 445, 4335
Gerhard O., Arnaboldi M., Freeman K. C., Okamura S., 2002, ApJ, 580, L121
González J. J., Cepa J., González-Serrano J. I., Sánchez-Portal M., 2014, MNRAS, 443, 3289
Gonçalves D., Magrini L., Teodorescu A. M., Carneiro C. C., 2014, MN-RAS, 444, 1705
Haardt F., Madau P., 1996, ApJ, 461, 20
Haardt F., Madau P., 2012, ApJ, 746, 125
Hallenbeck G. et al., 2012, AJ, 144, 87
Hester J. A. et al., 2010, ApJ, 716, 14
Huang S., Haynes M. P., Giovanelli R., Brinchmann J., Stierwalt S., Neff S. G., 2012, ApJ, 143, 133
Hunt L., Dayal P., Magrini L., Ferrara A., 2016, MNRAS, 463, 2002
Iorio G., Fraternali F., Nipoti C., Di Teodoro E., Read J. I., Battaglia G., 2017, MNRAS, 466, 4159
James B. L., Koposov S., Stark D. P., Belokurov V., Pettini M., Olszewski E. W., 2015, MNRAS, 448, 2687
Janowiecki S. et al., 2015, ApJ, 801, 96
Kapferer W., Sluka C., Schindler S., Ferrari C., Ziegler B., 2009, A&A, 499, 87
Kenney J. P. D., Geha M., Jáchym P., Crowl H. H., Dague W., Chung A., van Gorkom J., Voomer B., 2014, ApJ, 780, 119
Kennicutt R. C., Jr, 1998, ARA&A, 36, 186
Kennicutt R. C., Bresolin F., Jr, French H., Martin P., 2000, ApJ, 537, 589
Kewley L. J., Dopita M. A., Sutherland R. S., Heisler C. A., Trevena J., 2001, ApJ, 556, 121
Kniazev A. Y., Pustilnik S. A., Zucker D. B., 2008, MNRAS, 384, 1045
Komatsu E. et al., 2009, ApJS, 180, 330
Kroupa P., Tout C. A., Gilmore G., 1993, MNRAS, 262, 545
Kwak K., Henley D. B., Shelton R. L., 2011, ApJ, 739, 30
Lamb M. P., Venn K. A., Shetrone M. D., Sakari C. M., Pritzl B. J., 2015, MNRAS, 448, 42

Lelli F., McGaugh S. S., Schombert J. M., 2016, ApJ, 816, 14
Marigo P. et al., 2017, ApJ, 835, 77
Marinacci F., Fraternali F., Nipoti C., Binney J., Ciotti L., Londrillo P., 2011, MNRAS, 415, 1534
McConnachie A. W., 2012, AJ, 144, 4
Murray S. D., White S. D. M., Blondin J. M., Lin D. N. C., 1993, ApJ, 407, 588
Navarro J. F., Frenk C. S., White S. D. M., 1996, ApJ, 462, 563
Oosterloo T., van Gorkom J., 2005, A&A, 437, L19
Osterbrock D. E., Ferland G. J., 2006, Astrophysics of Gaseous Nebulae and Active Galactic Nuclei, 2nd edn. University Science Books, Sausalito, CA
Pecaut M. J., Mamajek E. E., 2013, ApJS, 208, 9
Percival S. M., Salaris M., Cassisi S., Pietrinferni A., 2009, ApJ, 690, 427
Pettini M., Pagel B. E. J., 2004, MNRAS, 348, L59
Reines A. E., Nidever D. L., Whelan D. G., Johnson K. E., 2010, ApJ, 708, 26
Roediger J. C., Courteau S., 2015, MNRAS, 452, 3209
Romano D., Chiappini C., Matteucci F., Tosi M., 2005, A&A, 430, 491
Rosen A., Bregman J. N., 1995, ApJ, 440, 634
Roy N., Kanekar N., Braun R., Chengalur J. N., 2013, MNRAS, 436, 2352
Ryan-Weber E. V. et al., 2004, AJ, 127, 1431
Salpeter E. E., 1955, ApJ, 121, 161
Sand D. J. et al., 2015, ApJ, 806, 95 (S15)
Sand D. J. et al., 2017, ApJ, 843, 134 (S17)
Saul D. R. et al., 2012, ApJ, 758, 44
Scalo J. M., 1986, Fundam. Cosm. Phys., 11, 1
Scalo J., 1998, The Stellar Initial Mass Function (38th Herstmonceux Conference), 142, 201
Scannapieco E., Brüggen M., 2015, ApJ, 805, 158
Spitzer L., 1956, Physics of Fully Ionised Gases, Interscience Publishers, New York
Stone J. M., Gardiner T. A., Teuben P., Hawley J. F., Simon J. B., 2008, ApJS, 178, 137
Sweet S. M., Drinkwater M. J., Meurer G., Bekki K., 2014, ApJ, 782, 35
Tamura N., Sharples R. M., Arimoto N., Onodera M., Ohta K., Yamada Y., 2006, MNRAS, 373, 301
Taylor R., Davies J. I., Auld R., Minchin R. F., Smith R., 2013, MNRAS, 428, 459
Taylor R., Davies J. I., Jáchym P., Keenan O., Minchin R. F., Palou J., Smith R., Wnsch R., 2017, MNRAS, 467, 3648
Teyssier R., 2002, A&A, 385, 337
Theuns T., Leonard A., Efstathiou G., Pearce F. R., Thomas P. A., 1998, MNRAS, 301, 478
Tinsley B. M., 1980, Fundam. Cosm. Phys., 5, 287
Urban O., Werner N., Simionescu A., Allen S. W., Böhringer H., 2011, MNRAS, 414, 2101
Walborn N. R. et al., 2014, A&A, 564, A40
Williams B. F., Ciardullo R., Durrell P. R., 2007, A&A, 656, 756
Willman B., Strader J., 2012, AJ, 144, 76
Wolfire M. G., McKee C. F., Hollenbach D., Tielens A. G. G. M., 2003, ApJ, 587, 278
Yoshida M., Yagi M., Komiyama Y., Furusawa H., Kishikawa N., Hattori T., Okamura S., 2012, ApJ, 749, 43
Zanstra H., 1931, Z. Astrophys., 2, 1

This paper has been typeset from a TeX/LaTeX file prepared by the author.